Sensitivity of convective cell dynamics and microphysics to model resolution for the OWLeS IOP2b lake-effect snowband

Anders A. Jensen*

National Center for Atmospheric Research, Boulder, Colorado

Philip T. Bergmaier

Department of Atmospheric Science, Wyoming University, Laramie, Wyoming

Bart Geerts

Department of Atmospheric Science, Wyoming University, Laramie, Wyoming

Hugh Morrison

National Center for Atmospheric Research, Boulder, Colorado

Leah S. Campbell

Department of Atmospheric Sciences, University of Utah, Salt Lake City, Utah

**Corresponding author address:* Anders A. Jensen, National Center for Atmospheric Research, 3090 Center Green Drive FL2 2052, Boulder, CO 80301.

E-mail: ajensen@ucar.edu

ABSTRACT

The OWLeS lake-effect IOP2b case is simulated using the Weather Research and Forecasting model (WRF) with a horizontal grid spacing of 148 m. The dynamics and microphysics of the simulated high-resolution snowband and a coarser resolution band from the parent nest (1.33-km horizontal grid spacing) are compared to radar and aircraft observations. The Ice Spheroids Habit Model with Aspect-ratio Evolution (ISHMAEL) microphysics is used which predicts the evolution of ice particle properties including shape, maximum diameter, density and fall speed. The microphysical changes within the band that occur when going from 1.33-km to 148-m grid spacing are explored. Improved representation of the dynamics at higher resolution leads to a better representation of the microphysics of the snowband compared to radar and aircraft observations. Stronger updrafts in the high-resolution grid lead to larger ice nucleation rates and produce ice particles that are more heavily rimed and thus more spherical, smaller (in terms of mean maximum diameter) and faster falling. These changes to the ice particle properties in the high-resolution grid limit aggregation rates and improve reflectivity compared to observations. Graupel, observed in the band at the surface, is produced in the strongest convective updrafts, but only at the higher resolution. Ultimately, the quantitative precipitation forecast is improved at two locations compared to radar-derived values. Additionally, the duration of heavy precipitation just onshore from the collapse of convection is better predicted.

1. Introduction

Lake-aligned, lake-effect snowbands, such as those observed over Lake Erie and Lake Ontario, often produce heavy snowfall downwind of the lake (Niziol et al. 1995; Veals and Steenburgh 2015). Snow accumulations may exceed 1.5 m in 48 h, with mere centimeters accumulating just a few kilometers away (Buffalo NY Weather Forecast Office 2019b). These significant snow accumulations cause power outages, collapsed roofs, impassible roads and stranded motorists and ultimately loss of life (Schmidlin 1993; Buffalo NY Weather Forecast Office 2019b). These bands are generally narrow ($\sim$ 20 km wide), and therefore, while band-scale circulations can be resolved by models with O(1 km) horizontal grid spacings (Steenburgh and Campbell 2017; Campbell and Steenburgh 2017; Bergmaier et al. 2017), finer-scale features, in particular embedded convection, cannot. Lake-effect snowband dynamics and the dynamical impacts on microphysics and precipitation are therefore not entirely represented in models that employ O(1 km) grid spacings. Knowledge gained from fine-scale modeling validated against observational studies of these localized events can be used to improve forecasts for society's benefit.

Both observations and numerical models have been employed to improve lake-effect snow forecasts, with a focus on heavy-precipitation events. Lasting, heavy snowfall tends to occur when winds blow parallel to the long axis of an elliptically shaped lake, e.g., Lakes Erie and Ontario (Holroyd 1971; Kristovich and Steve 1995; Niziol et al. 1995), which allows the lower atmosphere to humidify and destabilize and favors strong convergence along the length axis of the lake (McVehil and Peace 1965; Peace and Sykes 1966; Passarelli and Braham 1981; Niziol et al. 1995). These snowbands are referred to as long-lake-axis-parallel (LLAP, Steiger et al. 2013) bands. Owing to the specific synoptic conditions that LLAP bands require and the band-scale circulations required for maintenance, prior work has focused on understanding how synoptic conditions impact LLAP snowband formation (Holroyd 1971; Lavoie 1972; Hjelmfelt 1990) and the mechanisms by which snowbands form and evolve on meso-α-β scales. Once formed, band intensity and maintenance are tied to the nature of the cross-band circulations.

Observations have been used to analyze the formation and maintenance of LLAP bands including the importance of low-level convergence from both the land breeze (from opposite shores) and friction (McVehil and Peace 1965; Peace and Sykes 1966; Passarelli and Braham 1981). Additionally, observations have highlighted the increase in precipitation when snowbands interact with orography (Peace and Sykes 1966). More recently, coordinated observations during the Lake Ontario Winter Storms (LOWS) project (Reinking et al. 1993) and the Ontario Winter Lake-effect Systems (OWLeS) field campaign (Kristovich et al. 2017) have provided the data sets necessary to use in conjunction with models to improve the prediction of severe lake-effect snow. For example, Veals and Steenburgh (2015) used operational radar observations to conclude that LLAP bands are the second most common mode of precipitation over the Tug Hill located downwind of Lake Ontario, behind "broad coverage". Minder et al. (2015) used both Micro Rain Radars and an x-band profiling radar to determine that precipitation transitioned from convective to stratiform across the shoreline and further inland during the OWLeS IOP2b case (a 24-h LLAP-band event during which 103 cm of snow fell on Tug Hill). Their conclusion, that the $\sim$400 m high Tug Hill terrain did not invigorate the lake-effect convection onshore, was corroborated by Welsh et al. (2016) who used aircraft observations along with other measurements to study characteristics of the $\sim$3 km deep IOP2b LLAP band over the lake and onshore. They found updrafts of up to 10 m s^{-1} over the lake accompanied by heavily rimed snow. They also noted that convection collapsed onshore and in-cloud turbulence decreased, but snow particle sizes increased from stratiform ascent over the terrain and over a cold dome associated with the polar air mass that came around the south side of Lake Ontario and produced a land breeze front stretching from the southeast corner of the lake to the northeast, over Tug Hill. Campbell et al. (2016) looked at the impact of terrain during the IOP2b case and found that during times when the banding was weak and more broad in coverage, the orographic enhancement was strongest.

These observational studies motivated high resolution, O(1 km), modeling studies of the OWLeS IOP2b case to explore the impacts of Tug Hill on LLAP band snow accumulation (Campbell and Steenburgh 2017) and impacts of the mesoscale forcing mechanisms, in particular the shoreline geometry (Steenburgh and Campbell 2017) and the secondary solenoidal circulation in the LLAP band (Bergmaier et al. 2017). Steenburgh and Campbell (2017) used simulations of the IOP2b case to determine that the shoreline geometry along the southeast part of Lake Ontario produce a critical land-breeze front, consistent with Welsh et al. (2016). Campbell and Steenburgh (2017) used the same simulations to discern that this land breeze front interacted with Tug Hill to produce increased precipitation mainly through deposition and accretional growth of ice particles lifted over the density current and the hill. Bergmaier et al. (2017) found that these O(1 km) simulations capture the cross-band circulation very well, as confirmed by airborne vertical-plane dual-Doppler radar data collected along flight legs across the IOP2b LLAP band. They found this circulation to be thermally-induced and buoyancy-enhanced over the lake. Over land, the LLAP band circulation weakened but the land-breeze front had its own shallower asymmetric circulation. Additional modeling studies of other lake-effect snow cases have looked at the impacts of lake ice coverage on the location and intensity of precipitation (Wright et al. 2013), the impacts of different boundary layer and surface layer schemes on precipitation (Conrick et al. 2015; Fujisaki-Manome et al. 2017), the sensitivity of precipitation characteristics to various microphysics schemes (Reeves and Dawson 2013), and the impact of regional data assimilation on lake-effect snow forecasts (Saslo and Greybush 2017).

The above studies have provided insight into lake-effect storms and the controls on precipitation location and intensity, but all of these modeling studies used O(1 km) horizontal grid spacings. Thus, the interaction between the snowband dynamics and microphysics and how precipitation characteristics change at higher resolutions has not been explored. Airborne cloud radar data shown in Welsh et al. (2016) and Bergmaier et al. (2017) at a resolution of O(10 m) reveal ubiquitous convective updrafts over the lake (both within the LLAP band and laterally, under the LLAP band anvil) at scales that cannot be captured by a 1-km, convection-permitting simulation. The issue at hand is relevant to our understanding of gray-zone dynamics, when updrafts are not fully resolved, and how this impacts the microphysics.

Additionally, there are questions as to how improvements to the dynamical representation of a simulated lake-effect snowband (though increased model resolution) impact its microphysical evolution and ultimately the distribution and intensity of lake-effect snowfall, and how the LLAP band forms and evolves in a high resolution simulation without a planetary boundary layer (PBL) parameterization. Finally, moving to higher resolution modeling will enable the exploration of the lesser known aspects of lake-effect systems, including the interaction between shallow helical-roll convection, which first forms near the upwind shore, and the deeper lake-scale LLAP circulation, which forms further downwind.

In this study, the OWLeS IOP2b case is simulated using a nested model configuration with a 148-m horizontal grid spacing inner domain. Model output is compared to radar and aircraft. Differences in the microphysics and dynamics of the band between the 148-m domain and its parent domain (1.33-km horizontal grid spacing) are explored. In section 2 we describe the IOP2b event, the observations, and the model. Comparisons of model output to the observations are discussed in section 3, and the impact of fine-scale model dynamics on the microphysical evolution of the band are discussed in section 4. A summary and conclusions are discussed in section 5.

2. The OWLeS IOP2b lake-effect case

a. Synoptic overview

At 0000 UTC 11 December 2013, an intense LLAP band formed and heavy snow fell for the next 24 h (Steenburgh and Campbell 2017). The snowband was associated with a persistent upper-level trough bringing Arctic air to the region. By 1800 UTC 11 December 2013, North American Regional Reanalysis (NARR) data showed that 850-mb temperatures were $-16\,^{\circ}$C over Lake Ontario and the 850-mb geostrophic wind was parallel to the long axis of the lake (Fig. 1). One hundred twelve centimeters of snow was reported in Redfield, New York, in 24 h (Buffalo NY Weather Forecast Office 2019a). A more complete synoptic description of the event can be found in Campbell et al. (2016).

b. Observations

Radar observations used in this study were obtained from the KTYX NEXRAD S-band (10 cm) radar located in Montague, New York (NOAA National Weather Service (NWS) Radar Operations Center 1991). The KTYX radar variables used are the Level II base reflectivity, the Level III Digital Precipitation Rate (DPR/176) and the Level III One-Hour Precipitation (DAA/170). The latter two products are based not just on reflectivity, but also dual-polarization values, and have been validated extensively against precipitation gauges, though mainly in Oklahoma (Ryzhkov et al. 2005). In essence, the radar echoes first are identified (e.g., hail, dry snow, wet snow, biological targets, clutter ...) and then hydrometeor-specific relationships with precipitation rate are used (Park et al. 2009). All plots using KTYX observations are made using Py-ART (Helmus and Collis 2016).

Airborne in situ and remote sensing observations utilized in this study were obtained from instrumentation aboard the University of Wyoming King Air (UWKA) research aircraft. Rodi (2011) and Wang et al. (2012) discuss the measurement capabilities of the UWKA in great depth. Flight level in situ measurements include temperature, air pressure, humidity, the 3D wind components, cloud and precipitation particle size distributions, and precipitation particle 2D imaging. In terms of remote sensing, the multi-antenna W-band (3-mm wavelength) Wyoming Cloud Radar (WCR) was mounted aboard the UWKA during OWLeS and provided vertical cross sections of radar reflectivity and Doppler velocity along flight tracks. W-band radars provide very high spatial resolution, but their signal attenuates in the presence of much cloud liquid water, and scattering by hydrometeors larger than ~ 1 mm falls in the Mie regime (Kollias et al. 2007). This study utilizes WCR measurements from only the near-zenith and near-nadir beams (hereafter the “up” and “down” beams, respectively), which were obtained quasi-simultaneously and sampled at 20 Hz along the flight track and every 15 m along the beams. The maximum unambiguous Doppler velocity is ± 15.8 m s^{-1} and the minimum detectable signal for both beams at a range of 1 km is about -33 dBZ (Wang et al. 2012).

The aircraft motion was removed from the WCR Doppler velocity measurements when UWKA attitude angles caused the beams to deviate from the vertical. The wind profile from a nearby sounding was also used to further correct for horizontal wind contamination arising from off-vertical antenna pointing angles, due to these attitude deviations. Following these corrections, the resulting velocity measurements from the two beams provide the profile of hydrometeor vertical velocity above and below the aircraft. For a more thorough description of how WCR velocities were processed along flight tracks across the LLAP band (and across the primary wind) during OWLeS, see Welsh et al. (2016) and Bergmaier et al. (2017).

Particle size distributions were measured aboard the UWKA by two optical array probes during OWLeS, each sorting particles into 101 bins of equal width: a Cloud Imaging Probe (CIP, sizing 0.01 – 2.51 mm, 25 micron bin width) and a 2D-Precipitation probe (2D-P, sizing 0.1 – 20.1 mm, 0.2 mm bin width). CIP's first two size bins are ignored because they lack reliability, thus the minimum size used here is 0.06 mm. The size of snow particles is complex; particle probe sizes mentioned in this study refer to the maximum 2D dimension.

c. WRF simulation setup

This study uses the Advanced Weather Research and Forecast (WRF) model version 3.8.1 run on the Cheyenne high-performance computer (Computational and Information Systems Laboratory 2007). The WRF model dynamics are fully compressible and non-hydrostatic, and the prognostic equations are time-integrated using a 3rd-order Runge-Kutta method. Four domains are used in a nested configuration (Fig. 2a) with horizontal grid spacings of 12 km for domain 1 (d01), 4 km for domain 2 (d02), 1.33 km for domain 3 (d03) and 148 m for domain 4 (d04). Seventy-nine vertical levels are used on a stretched vertical grid with 29 vertical levels in the first 3 km AGL. The advective timesteps used are 54 s, 18 s, 6 s and 1 s for each of the domains. Model output is written every ten minutes for d03 and every 5 minutes for d04. The domain top is at 50 hPa and is rigid with a Rayleigh damping layer applied to the uppermost 5 km. All four domains are initialized at 1200 UTC 10 December 2013, and the analysis period, following a 12-h spin-up, is from 0000 – 2200 UTC 11 December 2013.

The model setup for domains 1-3 is similar to the setup used by Campbell and Steenburgh (2017). Terrain in domains 1-3 is obtained using the U.S. Geological Survey (USGS) 30-second data. Additionally, these domains use the YSU PBL scheme (Hong et al. 2006) and first-order turbulence closure. The Kain-Fritsch cumulus parameterization (Kain 2004) is used on domain 1 and calculates moisture tendencies for cloud water and rain but not ice. Domain 4 is setup to run in large-eddy simulation (LES) mode in WRF. In LES mode, a 1.5-order turbulence closure scheme is used, the PBL scheme is turned off and diffusion is used for vertical mixing. This domain uses the Shuttle Radar Topography Mission (SRTM, Farr et al. 2007) 3-arcsecond (90-m) terrain dataset (Fig. 2b). Random potential-temperature perturbations with maximum magnitude of 0.01 K are added to the 36 westernmost domain 4 tiles and up to 700 mb to reduce the turbulence spinup time on the upwind boundary (Mirocha et al. 2014). Analysis of energy spectra (not shown) reveals that turbulence is spun up by Prince Edward Country, Ontario. Domain 4 (d04) will be referred to as the WRF-LES domain. Note that two-way feedback between domains is turned off, though a sensitivity study (not shown) with feedback on shows little difference in the evolution of the WRF-LES domain snowband. Turning off two-way feedback allows for cleaner testing of sensitivity to the grid spacings in domains 3 and 4.

All four domains use the unified Noah land-surface model, the Monin-Obukhov surface layer parameterization, the Rapid Radiative Transfer Model for GCMs (RRTMG, Iacono et al. 2008) and Jensen ISHMAEL microphysics[1]. The Jensen Ice-Spheroids Habit Model with Aspect-ratio Evolution (ISHMAEL) bulk microphysics scheme (Jensen and Harrington 2015; Jensen et al. 2017, 2018a,b) predicts the evolution of ice particle shape for two ice species, planar-nucleated (ice-one) and columnar-nucleated (ice-two) particles. Additionally, a third ice species, aggregates, is predicted. All three ice species are modeled using spheroids. In ISHMAEL microphysics, ice particle properties including shape, density, maximum dimension and fallspeed are predicted. Thus, improvements to the dynamical representation of the simulated lake-effect snowband in the WRF-LES domain can be directly linked to changes in microphysical processes (e.g. nucleation,

[1] The Jensen ISHMAEL microphysics is publicly available as of WRF Version 4.1, mp_physics = 55.

vapor growth, riming, aggregation) and how these changes impact ice particle properties. Both shortwave and longwave radiation are coupled to the microphysics.

Lake-surface temperatures for all domains are updated every 6 h from the Great Lakes Environmental Research Laboratory (GLERL) following Campbell and Steenburgh (2017). Additionally, ice cover is set manually based on information from the GLERL ice-cover analysis for domains 1-3 following Campbell and Steenburgh (2017). Lake Ontario was nearly ice free during the period of interest, though a few grid boxes in domain 3 are specified as ice-covered in Prince Edward Bay, Chaumont Bay, and Henderson Harbor. For simplicity, no lake ice is specified in the WRF-LES domain. We do not expect this to impact our results considering that the ice coverage in those bays is sparse, Prince Edward Bay is near the boundary of the WRF-LES domain, and the band is generally south of those bays during the analysis time.

3. Observation and WRF-model output comparison

WRF-model output from both the 1.33-km domain (d03) and the 148-m domain (d04, WRF-LES domain) is compared to radar and aircraft observations. Radar observations are used to evaluate the band-scale to convective scale elements in the snowband. Aircraft observations are used to explore the finer-scale dynamics and microphysics within the band. Model-observation comparisons are used to determine the dynamical and microphysical impacts that occurs when smaller scales are resolved in this lake-effect snowband simulation.

a. Band-scale evaluation using KTYX radar observations

From 0000-2200 UTC, the region atop Tug Hill received more than 48 mm of liquid with isolated regions receiving 64 mm (Fig. 3b), according to the KTYX base reflectivity field. Radar-derived liquid-equivalent precipitation is diagnosed from a power-law relationship with reflectivity. The same equation that was used by Campbell et al. (2016), from Vasiloff (2001), is used here, where $Z = 75S^2$ and where Z is the reflectivity factor in mm^6 m^{-3} and S is the liquid-equivalent precipitation rate in mm h^{-1}. This equation yields 24-h precipitation amounts that are within 1 mm of manual observations at Sand Creek, but it underestimates precipitation at North Redfield by 23% (Campbell et al. 2016). The Level II derived precipitation amounts were verified with surface observations using a heated Noah ETI weighing precipitation gauge with a single Alter-style windshield (Campbell et al. 2016). Undercatchment could be an issue when verifying against surface observations (Rasmussen et al. 2012), and therefore we also use Level III precipitation products. The Level III One-Hour Precipitation product has a similar spatial distribution of precipitation compared to the Z-S relationship but higher 22 h totals (Fig. 3b, dashed contours). Unfortunately, the accuracy of this product for lake-effect snow events is unknown.

Both the WRF-LES domain (Fig 3a.) and d03 (not shown) capture the total accumulated precipitation over the entire 22 hour period (also, see Campbell and Steenburgh 2017). The main difference between the WRF-LES domain and d03 is in the spatial distribution of the largest precipitation amounts on Tug Hill. There is a banded region where accumulations exceed 60 mm in d03 (Fig. 3a, cyan contour), as there is in the simulation by Campbell and Steenburgh (2017). In contrast, this region has a greater north-south extent in the WRF-LES domain, in better agreement with observations. The WRF-LES domain also produces slightly better precipitation amounts at Sandy Creek (27 mm) compared to d03, which produces 24 mm of liquid at Sandy Creek (8 mm less than the Level II radar-derived value). The WRF-LES domain produces 54 mm at North Redfield, in better agreement with the KTYX Level II radar-derived value compared to d03 (which produces 57 mm of liquid at North Redfield) but slightly worse when compared to the disaggregated observations (Table 1). The Level III precipitation product has higher precipitation totals at both Sandy Creek and North Redfield compared to all other observations and model output (Table 1).

During the event, the snowband varied in appearance on radar. At 0100 UTC 11 December 2013, snow detected by the KTYX radar began to intensify and a coherent band began to form. By 0220 UTC 11 December 2013, the band appeared rather contorted, and maximum reflectivity values of 30-35 dBZ were observed onshore and on the windward side of Tug Hill (Fig. 4c). Sixteen and a half hours later, at 1850 UTC 11 December 2013, the KTYX radar displayed a more linear primary snowband that extended from Lake Ontario, over the leeward side of Tug Hill, to the Ha-De-Ron-Dah Wilderness (Fig. 4f). Reflectivity values of 30-35 dBZ angled to the northeast across Tug Hill because the shoreline orientation near Oswego, New York produced land-breeze convergence there in a southwest-to-northeast orientation (see Fig. 7a and Steenburgh and Campbell 2017). A much weaker, second band can be seen to the north of the main band, and this second band formed due to a convergence zone along the northern shoreline of Lake Ontario (see Fig. 7a and Steenburgh and Campbell 2017). Convective cells with reflectivity values of 30 dBZ are embedded in the band at 1850 UTC over the lake and just onshore. A continuous region with reflectivity values of 30 dBZ cover the top of Tug Hill south of the radar location.

The d03 (Fig. 4a, d) and WRF-LES (Fig. 4b, e) reflectivity fields show similar band morphology: by 0220 UTC, the simulated bands are contorted and widen onshore, and by 1850 UTC the simulated bands become linear. By 1850 UTC, the band is shifted southward in both domains compared to the observations, which also occurred at this time in the simulation by Bergmaier et al. (2017). The model-derived reflectivity field is calculated to optimally represent the KTYX observations: we assume a 10-cm radar wavelength, and a 0.5° tilt angle from the location and elevation of KTYX (radar range-height circles are shown in Fig. 4e). The main difference between the WRF-LES domain and d03 is that the WRF-LES domain (d04) captures the band's mesoscale morphology and convective nature better than the 1.33 km simulation (d03). Convective cells with reflectivity values of 30 dBZ are embedded in the band in the WRF-LES domain, and similar to the observations, the areal extent of reflectivity values greater than 30 dBZ expands onshore. In contrast, the d03 band has one continuous region that extends from the lake to the windward side of Tug Hill where reflectivity values are greater than 30 dBZ. Domain 3 is more intense than the WRF-LES domain with widespread reflectivity values greater than 30 dBZ, but there are no signs of convective cells embedded in this band. The d03 band is similar in appearance to bands simulated by Bergmaier et al. (2017, their Fig. 2b) and Campbell and Steenburgh (2017, their Fig. 3f), which both used the same simulation with an inner domain with 1.33-km horizontal grid spacing.

The coherent, banded region of reflectivity in d03 is a persistent feature. Domain 3 has an extended region from the lake to Tug Hill where reflectivity values are 20 dBZ or greater 70% of the time (Fig. 5a) and a narrow, banded region where reflectivity values are 30 dBZ or greater 30% of the time (Fig. 5d). Frequencies of reflectivity values greater than 20 dBZ from both the KTXY radar (Fig. 5c) and the WRF-LES domain (Fig. 5b) increase going onshore with maximum values corresponding with the highest terrain on Tug Hill. Additionally, there is a broad region in the observations over Tug Hill where 10-30% of the time reflectivity values are 30 dBZ or greater. This region is shifted to the west in the WRF-LES domain (Fig. 5e). The largest ice particles (with largest reflectivity values) are deposited more frequently on Tug Hill in the observations and the WRF-LES domain, whereas the largest particles are more frequently deposited along the band and closer to the lake shore in d03.

Probability density plots of reflectivity values at both Sandy Creek (Fig. 6a) and North Redfield (Fig. 6b) confirm that d03 has a high bias in reflectivity values, whereas the probability of reflectivity values from the WRF-LES domain agrees better with the observations, especially at values greater than 25 dBZ. At Sandy Creek, d03 has a low bias in the probability of reflectivity values between 10-15 dBZ compared to observations and a high bias in the probability of reflectivity values between 30-35 dBZ. This implies that d03 has a mean particle size that tends to be biased high. At North Redfield, the observed and WRF-LES domain peaks in the probability of reflectivity values are between 25-30 dBZ, whereas d03 has a peak between 30-35 dBZ.

The above analysis shows one of the impacts on the snowband structure that occurs when reducing the simulation horizontal grid spacing. The horizontal grid spacing used in d03 is too large to resolve the convective cells embedded in the band. This directly impacts the snowband structure as seen in the reflectivity field comparison to observations. Convective cells on radar are approximately 1-2 km in diameter as a best estimate, comparable to the sizes of Sodus Bay and the North Sandy Pond. The convective cells that are resolved in the WRF-LES domain and not in d03 have two impacts on the band as inferred by the comparison to radar observations.

First, convective cells hinder the aggregation process by increasing ice nucleation and riming rates, thus limiting increases in mean particle size and reducing reflectivity values along the band. Nucleation generally occurs near the top of the band (see Fig. 13), and in regions where nucleation occurs in ISHMAEL microphysics, small, spherical ice is produced which reduces the bulk size of an ice distribution and makes the ice particles more spherical on average. In ISHMAEL, a particle size distribution shape is assumed, and therefore, nucleation (adding small particles) can reduce the mean size of a distribution. Physically, adding particles to a distribution would not impact in situ aggregation rates. Regardless, these newly nucleated particles will need time to grow by vapor deposition to sizes that can collect.

Additionally, riming causes ice particles to become more spherical. Smaller, more spherical particles collect with a smaller efficiency that larger, more eccentric particles (Connolly et al. 2012). These processes shift the distribution of reflectivity values towards lower ones in better agreement with observations (Fig. 6). The orographic and stratiform lift over Tug Hill is a weaker forcing than convective cells, which provides an environment with significant vapor growth, less riming and more aggregation (Campbell and Steenburgh 2017). Thus we expect and do see the highest reflectivity values over the terrain in the WRF-LES domain. Second, convective cells include narrow, strong up and downdrafts. These convective cells likely disrupt the band-scale circulation (see Bergmaier et al. 2017); the WRF-LES domain band is thus composed of convective cells in a banded orientation.

The main snowband forms along the southern shore land-breeze front (LBF1 Steenburgh and Campbell 2017) as shown in Fig. 7a. The vertical air motion at 1-km AGL is averaged from 1600-1800 UTC (during which the band is linear and nearly stationary) for the two domains. The band-averaged updraft is stronger in d03, particularly just onshore, even though updrafts within individual cells are stronger in the WRF-LES domain. Onshore, average vertical motion from d03 is as high as 2.75 m s^{-1} (Fig. 7b), whereas average vertical motion onshore in the WRF-LES domain has a maximum of 2.2 m s^{-1} (Fig. 7d).

In contrast to what occurs along the main band, the mid-lake convergence zone (dashed line between LBF1 and the CZ in Fig. 7c) and the northern shore convergence zone (CZ) are weaker in d03 than the WRF-LES domain (Fig. 7). The band of vertical motion in the middle of the lake in the WRF-LES domain is not seen in d03 over the lake. This mid-lake band is also seen as a convergence feature at 1800 UTC in the simulations of Steenburgh and Campbell (2017), and it produces an updraft of 0.5 m s^{-1} and reflectivity values over the lake of 10-20 dBZ in their simulation. This convergence zone is not related to a land-breeze front (Steenburgh and Campbell 2017); it is a center-of-the-lake solenoidal circulation. These convergence zones, the v-wind components, and the averaged vertical motions are stronger in the WRF-LES domain over the lake (Fig. 7a, c). The onshore merger of the main band, the northern shore convergence zone (CZ) and the mid-lake circulation (along with frictional convergence) produce a wide region onshore with updrafts that are stronger than in d03 (Fig. 7b, d).

The prominence of a single, dominant band-scale circulation in d03 exists both over the water (leg 3, Fig. 8a) and just onshore (leg 4, Fig. 8c). In fact, the d03 circulation strengthens onshore (Fig. 8c) due to the merger of several convergence zones there (Fig. 7a). On average, the main band is narrower in the WRF-LES domain over the lake compared to d03 (Fig. 8a, b, compared heating rates and red-shaded region). In contrast to what happens in d03, the strong, narrow convergence zone over the lake in the WRF-LES domain collapses onshore and merges with the other convergence zones north of it (Fig. 8c). The collapse of convection onshore (Welsh et al. 2016) is seen in the WRF-LES as the largest vertical air motions and heating rates disappear roughly 10 km onshore (Fig. 8d). The collapsed convective elements from the main band remain upright and deeper than the merged updrafts north of the main band.

The dynamical picture shown above supports the radar analysis: A strong main band dominates in d03, which is conducive for the growth and collection of ice to form large aggregates along the band. In contrast, the stronger, narrower convective elements in the WRF-LES domain both break up the band-scale circulation and hinder the aggregation process. The merger and collapse of convection onshore in the WRF-LES domain helps explain why the concentrated area of high reflectivity values in convective cores expands onshore in areas when the cells collapse.

b. Fine-scale band evaluation from aircraft observations

The radar evaluation of the band suggests that the convective elements in the band impact its microphysical evolution. Thus, we evaluate the fine-scale dynamics from aircraft observations to confirm if this is in fact the case. Additionally, we explore the extent to which the WRF-LES domain captures the fine-scale dynamics in the band.

The hydrometeor vertical velocity field *w* (a combination of vertical air motion and reflectivity-weighted particle fall speed) is measured directly by the WCR. We use this field to analyze the fine-scale dynamics (and microphysics) of the snow band. To compare the model hydrometeor vertical velocity to the WCR hydrometeor vertical velocity, reflectivity-weighted fall speeds (see Molthan et al. 2016) are output for each of the three ice species in ISHMAEL microphysics. A reflectivity-weighted average (using the reflectivity factor) of these three fall speeds is then computed as a total average value of the reflectivity-weighted fall speed. This value is combined with the vertical air motion from WRF to compute *w* from the model.

Distributions of *w* from the model are sampled along each flight leg (see Fig. 2b) at 1 km AGL from both 1600-1800 UTC (model time), when the simulated band is closer in location to the observed band at 1850 UTC, and 1800-2000 UTC, when the simulated band is slightly farther south than the observed band (see Fig. 4). During both time periods, the band is linear. Distributions of WCR *w* for each flight leg contain transects flown between 1905-2029 UTC. Four transects were used for leg 3 (over water), three for leg 4 (over the western foothills of Tug Hill), and one for leg 5 (over Tug Hill).

The WCR *w* distribution becomes progressively more narrow going onshore (Fig. 9a-c, black line). The peak of this distribution is near -1 m s^{-1} for each leg which corresponds to ice particles falling at 1 m s^{-1}, the approximate fall speed of aggregates (Locatelli and Hobbs 1974). Over the lake (leg 3) at 1 km AGL, updrafts of over 7.5 m s^{-1} were measured, and updrafts of 10 m s^{-1} were measured over the lake up to 3 km MSL (Welsh et al. 2016). The distribution of WCR *w* over the lake (Fig 9a) is positively skewed: downward *w* values are not as large in magnitude as upward values. This is characteristic of boundary-layer moist convection (Zhu and Zuidema 2009; Ghate et al. 2010; Lamer and Kollias 2015). Onshore the vertical velocity distribution becomes less skewed and narrower with values ranging from approximately ± 3 m s^{-1} over the windward side of Tug Hill (leg 5, Fig. 9c).

Compared to the WCR *w*, the WRF-LES domain captures the distribution of the up and downdrafts from 1600-1800 UTC along legs 3 (Fig. 9a, orange line) and 4 (Fig. 9b, orange line), whereas d03 cannot capture the larger values of the up and downdrafts over the lake, with peak updrafts of approximately 3 m s^{-1} (Fig. 9a, blue line), in agreement with Bergmaier et al. (2017). The *w* distributions are too narrow for both d03 and the WRF-LES domain compared to observations for leg 5 (Fig. 9c), though the WRF-LES domain has a wider *w* distribution in better agreement with observations. The discrepancy between the observations and the WRF-LES domain along leg 5 are likely caused by the complicated nature of the band over land. The combination of the orography (Campbell and Steenburgh 2017), the land-breeze fronts (Steenburgh and Campbell 2017) and the collapse of convection (Welsh et al. 2016) all complicate the onshore dynamics. The WRF-LES domain compares better to the observations at 1600-1800 UTC than at 1800-2000 UTC (Fig. 9c, f) when the simulated band is closer in location (farther north) to the observed band. Thus, the distribution of *w* over Tug Hill (leg 5) is likely still influenced by convection (or the collapse thereof) in the band.

The WCR *w* spectra are compared to values computed from the WRF-LES domain over both the lake and onshore at 1 km AGL (Fig. 10). The *w* spectra are computed from model output using the same *w* values computed for Fig. 9. Power spectra are computed along two tracks, corresponding with flight legs 3 (Fig. 10a) and 5 (Fig. 10b), at each model output time from 1600-1800 UTC, and then those spectra are averaged and plotted. This is repeated for the time period 1800-2000 UTC. The sampling frequency of the modeled spectra is calculated assuming that an aircraft is flying through the domain at 100 m s^{-1}. Over the lake, the model has similar power spectral densities comparing 1600-1800 and 1800-2000 UTC, but over land (leg 5), the power decreases at the later time in agreement with weaker updrafts (Fig. 9c, f). The inertial subrange is appropriately characterized by the WRF-LES domain down to about 1-km ($6-7\ \Delta x$, Skamarock 2004) over both the lake and land.

One way to determine how the dynamics and the microphysics are coupled in the lake-effect band involves analyzing how reflectivity Z varies with hydrometeor vertical velocity w. Specifically, this reveals the coupling between updrafts which produce ice and the location of the largest ice particles. WCR $Z-w$ frequency plots (from 0-1 km AGL) along legs 3 (Fig. 11c) and 5 (Fig. 11f) reveal a strong negative correlation between Z and w over the lake (magenta box) and a much weaker but still negative correlation over land. The negative correlation between Z and w over the lake implies that strong updrafts contain fewer larger ice particles which are being lofted from the tops of these strong updrafts (bounded weak echo regions, BWERs) in a "fountain effect" (see Welsh et al. 2016, their Figs. 7c, 8c) and (see Bergmaier et al. 2017, their Fig. 6a, b). Over land, a much weaker correlation between Z and w exists in part because up and downdraft strengths are weaker.

Similar $Z-w$ frequency plots created from model output over 1600-2000 UTC and 0-1 km AGL to attain a large sample for both d03 and the WRF-LES domain are shown in Fig. 11a, b. The model reflectivity (assumed 10-cm wavelength) cannot be directly compared to the WCR (3-mm) radar, especially since the WCR (a W-band radar) reflectivity starts to plateau around 10-15 dBZ on account of Mie scattering and path-integrated attenuation (Kollias et al. 2007; Matrosov and Battaglia 2009). Nevertheless, similar results are expected from the model output: sufficiently strong updrafts should loft ice particles and be associated with lower reflectivity values.

The WRF-LES domain shows a weaker negative $Z-w$ correlation over the water (Fig. 11b, magenta box) than the observations, but a stronger correlation than d03 (Fig. 11a). Additionally, the WRF-LES domain has a larger spread in w over both the lake and land compared to d03 (previously shown in Fig. 9). The difference between d03 and the WRF-LES domain is that the average w decreases in the WRF-LES domain between Z values of 0 to 18 dBZ, in a more similar fashion compared to the observations. This is evidence that the coupling between the microphysics and dynamics in the WRF-LES domain is working in the right direction for $Z < 20$ dBZ, where the largest of these particles are pushed out of the top of the strongest updrafts over the lake in a “fountain effect”. Over land, the updrafts in both d03 and the WRF-LES domain are weaker and there is less of a $Z - w$ correlation, in agreement with observations. As noted, the w distribution is too narrow over land for the WRF-LES domain; this is also seen in the analysis of $Z - w$. The WRF-LES domain and d03 over both the lake and land show a spike in w corresponding with $Z = 25$ dBZ. This spike is caused by aggregates, which also tend to correspond with positive (upward) w.

In addition to evaluating the simulation based on WCR w, another way to evaluate the simulated microphysical evolution of the band is through a model-observation comparison of ice particle size distributions. ISHMAEL is a bulk microphysics scheme with three ice species, all of which have fixed gamma distribution shape parameters of $\nu = 4$ (see Jensen et al. 2017). The three ice species are combined by binning the size distributions using 200 bins in the space of maximum diameter (D). A distribution is created for each model grid cell along a given flight leg from 1600-1800 UTC. An ice species must have a mass mixing ratio of greater than 0.001 g kg^{-1} to be included. For each D-bin, the spread between the 25$^{\text{th}}$ and 75$^{\text{th}}$ percentiles is shaded in Fig. 12.

Over the lake, observations show a general trend of the largest particles (> 3 mm) becoming more numerous with decreasing height (Fig. 12a, squares), and the WRF-LES domain shows a similar evolution (Fig. 12a, shaded regions). This suggests that the aggregation process is active over the lake, especially since 1-cm particles are observed there. The model has a high bias in number concentrations at $D = 1$ mm and a low bias in number concentration for particles with $D = 0.1$ mm compared to observation.

Additionally, the observations reveal that the number of large particles increases at 1.7 km MSL and just onshore (leg 4) in updrafts $w > 1$ m s^{-1} compared to the downdrafts $w < 0$ m s^{-1} (Fig. 12b). Again, the WRF-LES domain shows a similar result with a distinct separation in ice size distributions between the strong updrafts and all downdrafts. These onshore updrafts contain large particles (aggregates) with relatively low fall speeds which can be deposited downwind and continue to grow by vapor deposition and aggregation over Tug Hill (Campbell and Steenburgh 2017).

The model-observation comparison using aircraft observations including hydrometeor vertical velocity and ice size distributions demonstrates that the WRF-LES domain captures the stronger dynamics that occurs in the band compared to the 1.33-km domain. Additionally, the WRF-LES domain captures the general trends in the evolution of ice particle size distribution and the interaction between ice particles and the dynamics.

4. The impact of better-resolved lake-effect band dynamics on ice particle properties

It was shown that the WRF-LES domain captures both the dynamics and the microphysics of the lake-effect band compared to radar and aircraft observations. Thus, we explore the ice particle properties including the masses, sizes, shapes, fall speeds, densities, and number concentrations to determine the impact of the in-band convective elements on the microphysics. ISHMAEL microphysics is a particle property scheme, and therefore, ice particle properties are updated consistently by process rates such as vapor growth and riming (Jensen and Harrington 2015; Jensen et al. 2017). It is expected (as mentioned earlier) that stronger updrafts will produce higher ice number concentrations, more riming and fewer aggregates.

Larger values of ice number concentrations are produced in the WRF-LES domain from the stronger updrafts, particularly for ice-one (n_{I1}), which is planar-nucleated ice, compared to d03 (Table 2). These higher ice number concentrations occur along both legs 3 and 5 (Table 2). Both of the domains produce similar ice-one mass mixing ratios (q_{I1}). Ice-two mass and number concentrations are small because ice-two (columnar-nucleated ice) initiation occurs near $-7\,^{\circ}$C, which is near the surface and generally lower in elevation than where most of the ice nucleation occurs for this case. Aggregate mass concentrations are larger in d03 compared to the WRF-LES domain along both legs as expected.

At 1510 along a cross-section through Sandy Creek and 1600 UTC along leg 4, a single cross-band circulation exists in d03 (Fig. 13a, c). In contrast, the WRF-LES domain has a main circulation in which multiple updrafts are embedded (Fig. 13b, c). The single circulation seen in d03 is conducive to aggregate formation at 1600 UTC (Fig. 13c, high reflectivity values and the black line), whereas the main circulation is broken up in the WRF-LES domain and the stronger updrafts support larger ice number concentrations (Fig. 13b, d, white lines), pockets of aggregates and a more broken reflectivity field. Additionally, the "fountain effect" is evident in the WRF-LES domain at 1600 UTC near $y = 21$ km and $z = 1 - 1.5$ km (Fig. 13d, dark gray shaded region). Here the updraft (air motion) is greater than 5 m s^{-1} and the reflectivity values in the updraft are lower than those above it.

The dynamical differences that exist between d03 and the WRF-LES domains in general lead to higher ice number concentrations and more riming (more isometric ice particles) in the WRF-LES domain (Fig. 14a, b). The number-weighted aspect ratios (see Jensen et al. 2018a, their Eq. 5) are less than unity for planar (oblate) particles. The single cross-band circulation that occurs in d03 produces rimed and newly nucleated (Fig. 14a, white contour) and isometric particles ($\phi = 0.5$) near the top of the updraft and more eccentric (vapor-grown) particles elsewhere. These vapor-grown particles in d03 attain maximum diameters of up to 2 mm near the surface (Fig. 14c), attain fall speeds of less than 1 m s^{-1} (Fig. 14c, black lines) and have densities of 400 – 500 kg m^{-3} (Fig. 14a, black lines) which is typical of vapor-grown, branched, planar particles such as dendrites. Not surprisingly, this is where the aggregate mass mixing ratios and reflectivity values are the largest (Fig. 13a).

In contrast, the narrower, stronger updrafts in the WRF-LES domain cover a larger areal extent across the band than in d03 at 1510 UTC. This supports higher ice number concentrations aloft (Fig. 13b) and more rimed particles (Fig. 14b, white contours) with larger aspect ratios (Fig. 14b). These rimed particles have aspect ratios of 0.5 – 1.0 (Fig. 14b), densities of 300 – 400 kg m^{-3} (Fig. 14b, black contours) mass-weighted maximum diameters of 0.5-1 mm (Fig. 14d) and produce pockets of ice particles falling faster than 1 m s^{-1} (Fig. 14d, black contours). Rimed particles were observed at the tops of the strongest updrafts at 3 km MSL (Welsh et al. 2016); these particles exist in the WRF-LES domain but not in d03.

Table 3 reveals that at Sandy Creek for the duration of the event, a smaller percentage of aggregates fell in the WRF-LES domain than in d03. Additionally, a larger percentage of the ice that was not aggregates (ice-one) is less eccentric (more spherical). Additionally, updrafts are stronger in the WRF-LES domain at Sandy Creek than in d03. Welsh et al. (2016) used disdrometer data to estimate that 10% of the precipitation at Sandy Creek was graupel-like based on fall speeds, and the most probable particle size was a diameter of 0.5 mm. In the WRF-LES domain, 2.8% of the ice falling at Sandy Creek is ice-two and this ice is all quasi-spherical ($0.8 < \phi_{I2} < 1.2$). Seven percent of ice-one has aspect ratios greater than 0.25 and 1% of ice-one has aspect ratios greater than 0.5. Thus, 3.8% of ice at Sandy Creek in the WRF-LES domain is graupel and 9.8% is partially rimed (including graupel) based on particle shape.

Ultimately, the pockets of rimed particles produce narrow but significant increases in the vertical flux of ice near the surface at Sandy Creek at 1510 UTC (Fig. 15). While rimed particles may only account for a relatively small percentage of ice at the surface (at least for this case), those particles may help significantly increase precipitation rates locally for brief periods of time. Just onshore and over the lake (west of Sandy Creek), liquid equivalent precipitation rates estimated from Level II radar data exceed 4.23 mm h^{-1} (2 inches h^{-1} of snowfall assuming a 12-1 snow-to-liquid ratio) for 30-60 min (Fig. 16c); liquid equivalent precipitation rates from the Level III DPR product exceed 4.23 mm h^{-1} for about 180 min (Fig. 16c, brown contour line). The frequency of these heavy precipitation rates, which represent the most hazardous part of lake-effect snow storms, are matched better in the WRF-LES than in the d03 simulation. Also, they are seen in the same location in the WRF-LES domain (Fig. 16b) but are not seen in d03 (Fig. 16a), where precipitation rates this large and for at least 30 minutes do occur just onshore. Additionally, there is a large, banded region in d03 where precipitation rates exceed 4.23 mm h^{-1} for 6.5-7 h, which is not seen in the observations. In d03, the duration of relatively heavy snowfall is missed just onshore and is over-predicted for a banded region east of North Redfield. These differences are consistent with differences in the accumulated precipitation field seen in Fig. 3.

5. Conclusions

The OWLeS IOP2b case is simulated using a nested WRF configuration with the innermost domain utilizing 148 m horizontal grid spacing, which is nine-fold smaller than used in previous simulations of the case (Bergmaier et al. 2017; Campbell and Steenburgh 2017; Steenburgh and Campbell 2017). Results using this high-resolution WRF-LES domain are compared with those using a coarser 1.33-km horizontal grid spacing domain (d03). A direct result of the increased resolution is that the model is able to capture the strongest updrafts in the band, up to 7.5 m s^{-1}, in better agreement with aircraft observations of Doppler hydrometeor vertical velocity.

There are several changes that occur in the microphysical evolution of the band when stronger updrafts are resolved in the WRF-LES domain. These changes are apparent when comparing the simulations to radar observations. Stronger updrafts lead to increased ice nucleation rates and riming rates. These increases in ice number concentrations and rimed particles produce a higher fraction of ice that is not purely vapor grown, and because these more spherical particles collect with a lower efficiency than vapor grown ones, aggregation rates are reduced. Radar observations generally support this microphysical picture of the band at two locations onshore. The most probable reflectivity value onshore is less in the WRF-LES domain than the 1.33-km domain because aggregation rates are reduced, and because smaller, more numerous particles populate the band. Additionally, the stronger updrafts disrupt the cross band circulation, which is on average weaker onshore in the WRF-LES domain.

The overall realism of the d03 simulation in terms of its ability to capture the precipitation as well as the general reflectivity field implies that the band dynamics and the evolution of the microphysics including the impact on the reflectivity field are dominated by the band-scale (mesoscale) convergence. Nonetheless, differences between d03 and the WRF-LES domain in the reflectivity field highlight how better resolving lake-effect dynamics impacts the microphysics, including how stronger updrafts change the microphysics. Understanding the impact of better resolved dynamics on microphysics is important because both operational and research models are being run at increasingly higher resolution. The WRF-LES domain can be used also as an assessment of radar-based precipitation estimation in lake-effect snow storms. It appears that the NEXRAD dual-polarization Level III radar precipitation products overestimate the total precipitation in this case, in particular because of an overestimation of the heaviest snowfall rates. Though precipitation rates derived from the Level II data may underestimate precipitation.

As models are run at increasingly higher resolutions, a need to change or improve model parameterizations, such as microphysics, may be necessary. As found in this study, a shift in microphysical process rates occurs when more intense updrafts are resolved. It is beyond the scope of this work to determine how traditional microphysics schemes, which use pre-defined, discrete categories such as cloud ice, snow, and graupel, will handle higher resolutions for modeling lake effect snowbands. Traditional schemes must formulate conversion processes between categories, and these processes are often ad-hoc and based on thresholds that can lead to large, discrete changes in simulated clouds and precipitation (Morrison and Grabowski 2008). Thus, we hypothesize that traditional microphysics schemes may be more sensitive to changes in resolution; better resolving updrafts will increase riming rates which could tip snowband simulations from being snow-dominated to graupel-dominated. Schemes like ISHMAEL microphysics and P3 (Morrison and Milbrandt 2015) that eschew traditional ice categories and smoothly evolve ice particle properties like density and fallspeed may be more adept to handle increased model resolution. Testing this hypothesis is left to future work.

Acknowledgments. The authors thank the National Science Foundation's NSF-AGS postdoctoral research fellowship program (grant AGS-1524267) which was instrumental for this research. B. Geerts and P. Bergmaier acknowledge NSF grant AGS-1258856 and P. Bergmaier acknowledges NSF grant DUE-1821566. Implementation of the high-resolution terrain was made possible by the one and only Michael G. Duda. Discussions with Peter Sullivan about turbulence were enlightening. We are thankful for useful comments by James Pinto. We thank the UWKA flight crew for their hard work. NCEP Reanalysis data was provided by NOAA/OAR/ESRL PSD, Boulder, Colorado, USA, from their Web site at https://www.esrl.noaa.gov/psd/. The National Center for Atmospheric Research is sponsored by the National Science Foundation.

References

Bergmaier, P. T., B. Geerts, L. S. Campbell, and W. J. Steenburgh, 2017: The OWLeS IOP2b lake-effect snowstorm: Dynamics of the secondary circulation. *Monthly Weather Review*, **145 (7)**, 2437–2459, doi:10.1175/MWR-D-16-0462.1.

Buffalo NY Weather Forecast Office, 2019a: Lake Effect Snow Event Archive: Lake Effect Summary Dec 10-13 2013. URL https://www.weather.gov/buf/lesEventArchive?season=2013-2014&event=A.

Buffalo NY Weather Forecast Office, 2019b: Lake Effect Snow Event Archive: Lake Effect Summary Nov 17-19 2014. URL https://www.weather.gov/buf/lesEventArchive?season=2014-2015&event=B.

Campbell, L. S., and W. J. Steenburgh, 2017: The OWLeS IOP2b lake-effect snowstorm: Mechanisms contributing to the Tug Hill precipitation maximum. *Monthly Weather Review*, **145 (7)**, 2461–2478, doi:10.1175/MWR-D-16-0461.1.

Campbell, L. S., W. J. Steenburgh, P. G. Veals, T. W. Letcher, and J. R. Minder, 2016: Lake-effect mode and precipitation enhancement over the Tug Hill Plateau during OWLeS IOP2b. *Monthly Weather Review*, **144 (5)**, 1729–1748, doi:10.1175/MWR-D-15-0412.1.

Computational and Information Systems Laboratory, 2007: Cheyenne: Hpe/sgi ice xa system (university community computing). Boulder, CO: National Center for Atmospheric Research, doi:10.5065/D6RX99HX.

Connolly, P. J., C. Emersic, and P. R. Field, 2012: A laboratory investigation into the aggregation efficiency of small ice crystals. *Atmospheric Chemistry and Physics*, **12 (4)**, 2055–2076, doi:10.5194/acp-12-2055-2012.

Conrick, R., H. D. Reeves, and S. Zhong, 2015: The dependence of qpf on the choice of boundary- and surface-layer parameterization for a lake-effect snowstorm. *Journal of Applied Meteorology and Climatology*, **54 (6)**, 1177–1190, doi:10.1175/JAMC-D-14-0291.1.

Farr, T. G., and Coauthors, 2007: The shuttle radar topography mission. *Reviews of Geophysics*, **45 (2)**, doi:10.1029/2005RG000183.

Fujisaki-Manome, A., and Coauthors, 2017: Turbulent heat fluxes during an extreme lake-effect snow event. *Journal of Hydrometeorology*, **18 (12)**, 3145–3163, doi:10.1175/JHM-D-17-0062.1.

Ghate, V. P., B. A. Albrecht, and P. Kollias, 2010: Vertical velocity structure of nonprecipitating continental boundary layer stratocumulus clouds. *Journal of Geophysical Research: Atmospheres*, **115 (D13)**, doi:10.1029/2009JD013091.

Helmus, J. J., and S. M. Collis, 2016: The python arm radar toolkit (py-art), a library for working with weather radar data in the python programming language. *Journal of Open Research Software*, **4 (1)**, p.e25, doi:http://doi.org/10.5334/jors.119.

Hjelmfelt, M. R., 1990: Numerical study of the influence of environmental conditions on lake-effect snowstorms over lake michigan. *Monthly Weather Review*, **118 (1)**, 138–150, doi:10.1175/1520-0493(1990)118⟨0138:NSOTIO⟩2.0.CO;2.

Holroyd, E. W., 1971: Lake-effect cloud bands as seen from weather satellites. *Journal of the Atmospheric Sciences*, **28 (7)**, 1165–1170, doi:10.1175/1520-0469(1971)028⟨1165:LECBAS⟩2.0.CO;2.

Hong, S.-Y., Y. Noh, and J. Dudhia, 2006: A new vertical diffusion package with an explicit treatment of entrainment processes. *Monthly Weather Review*, **134 (9)**, 2318–2341, doi:10.1175/MWR3199.1.

Iacono, M. J., J. S. Delamere, E. J. Mlawer, M. W. Shephard, S. A. Clough, and W. D. Collins, 2008: Radiative forcing by long-lived greenhouse gases: Calculations with the aer radiative transfer models. *Journal of Geophysical Research: Atmospheres*, **113 (D13)**, doi:10.1029/2008JD009944.

Jensen, A. A., and J. Y. Harrington, 2015: Modeling ice crystal aspect ratio evolution during riming: A single-particle growth model. *J. Atmos. Sci.*, **72**, 2569–2590, doi:http://dx.doi.org/10.1175/JAS-D-14-0297.1.

Jensen, A. A., J. Y. Harrington, and H. Morrison, 2018a: Impacts of ice particle shape and density evolution on the distribution of orographic precipitation. *Journal of the Atmospheric Sciences*, **75 (9)**, 3095–3114, doi:10.1175/JAS-D-17-0400.1.

Jensen, A. A., J. Y. Harrington, and H. Morrison, 2018b: Microphysical characteristics of squall-line stratiform precipitation and transition zones simulated using an ice particle property-evolving model. *Monthly Weather Review*, **146 (3)**, 723–743, doi:10.1175/MWR-D-17-0215.1.

Jensen, A. A., J. Y. Harrington, H. Morrison, and J. A. Milbrandt, 2017: Predicting ice shape evolution in a bulk microphysics model. *Journal of the Atmospheric Sciences*, **74 (6)**, 2081–2104, doi:10.1175/JAS-D-16-0350.1.

Kain, J. S., 2004: The kain–fritsch convective parameterization: An update. *Journal of Applied Meteorology*, **43 (1)**, 170–181, doi:10.1175/1520-0450(2004)043⟨0170:TKCPAU⟩2.0.CO;2.

Kollias, P., E. E. Clothiaux, M. A. Miller, B. A. Albrecht, G. L. Stephens, and T. P. Ackerman, 2007: Millimeter-wavelength radars: New frontier in atmospheric cloud and precipitation research. *Bulletin of the American Meteorological Society*, **88 (10)**, 1608–1624, doi: 10.1175/BAMS-88-10-1608.

Kristovich, D. A. R., and R. A. Steve, 1995: A satellite study of cloud-band frequencies over the great lakes. *Journal of Applied Meteorology*, **34 (9)**, 2083–2090, doi:10.1175/1520-0450(1995)034⟨2083:ASSOCB⟩2.0.CO;2.

Kristovich, D. A. R., and Coauthors, 2017: The Ontario Winter Lake-effect Systems field campaign: Scientific and educational adventures to further our knowledge and prediction of lake-effect storms. *Bulletin of the American Meteorological Society*, **98 (2)**, 315–332, doi: 10.1175/BAMS-D-15-00034.1.

Lamer, K., and P. Kollias, 2015: Observations of fair-weather cumuli over land: Dynamical factors controlling cloud size and cover. *Geophysical Research Letters*, **42 (20)**, 8693–8701, doi:10.1002/2015GL064534.

Lavoie, R. L., 1972: A mesoscale numerical model of lake-fffect storms. *Journal of the Atmospheric Sciences*, **29 (6)**, 1025–1040, doi:10.1175/1520-0469(1972)029⟨1025:AMNMOL⟩2.0.CO;2.

Locatelli, J. D., and P. V. Hobbs, 1974: Fall speeds and masses of solid precipitation particles. *J. Geophys. Res.*, **79 (15)**, 2185–2197.

Matrosov, S. Y., and A. Battaglia, 2009: Influence of multiple scattering on cloudsat measurements in snow: A model study. *Geophysical Research Letters*, **36 (12)**, doi:10.1029/2009GL038704.

McVehil, G. E., and R. L. Peace, Jr., 1965: Some studies of lake effect snowfall from lake erie. *Proceedings of 8th Conference on Great Lakes Research*, University of Michigan, 262–272.

Minder, J. R., T. W. Letcher, L. S. Campbell, P. G. Veals, and W. J. Steenburgh, 2015: The evolution of lake-effect convection during landfall and orographic uplift as observed by profiling radars. *Monthly Weather Review*, **143 (11)**, 4422–4442, doi:10.1175/MWR-D-15-0117.1.

Mirocha, J., B. Kosović, and G. Kirkil, 2014: Resolved turbulence characteristics in large-eddy simulations nested within mesoscale simulations using the weather research and forecasting model. *Monthly Weather Review*, **142 (2)**, 806–831, doi:10.1175/MWR-D-13-00064.1.

Molthan, A. L., B. A. Colle, S. E. Yuter, and D. Stark, 2016: Comparisons of modeled and observed reflectivities and fall speeds for snowfall of varied riming degrees during winter storms on long island, new york. *Monthly Weather Review*, **144 (11)**, 4327–4347, doi:10.1175/MWR-D-15-0397.1.

Morrison, H., and W. W. Grabowski, 2008: A novel approach for representing ice microphysics in models: Description and tests using a kinematic framework. *J. Atmos. Sci.*, **65**, 1528–11 548.

Morrison, H., and J. A. Milbrandt, 2015: Parameterization of cloud microphysics based on the prediction of bulk ice particle properties. Part I: Scheme description and idealized tests. *J. Atmos. Sci.*, **72**, 287–311, doi:http://dx.doi.org/10.1175/JAS-D-14-0065.1.

Niziol, T. A., W. R. Snyder, and J. S. Waldstreicher, 1995: Winter weather forecasting throughout the eastern united states. part iv: Lake effect snow. *Weather and Forecasting*, **10 (1)**, 61–77, doi:10.1175/1520-0434(1995)010⟨0061:WWFTTE⟩2.0.CO;2.

NOAA National Weather Service (NWS) Radar Operations Center, 1991: Noaa next generation radar (NEXRAD) level 2 base data. KTYX. NOAA national centers for environmental information. Access date: 05 August 2017, doi:10.7289/V5W9574V.

Park, H. S., A. V. Ryzhkov, D. S. Zrnić, and K.-E. Kim, 2009: The hydrometeor classification algorithm for the polarimetric wsr-88d: Description and application to an mcs. *Weather and Forecasting*, **24 (3)**, 730–748, doi:10.1175/2008WAF2222205.1.

Passarelli, R. E., and R. R. Braham, 1981: The role of the winter land breeze in the formation of great lake snow storms. *Bulletin of the American Meteorological Society*, **62 (4)**, 482–491, doi:10.1175/1520-0477(1981)062⟨0482:TROTWL⟩2.0.CO;2.

Peace, R. L., and R. B. Sykes, 1966: Mesoscale study of a lake effect snow storm. *Monthly Weather Review*, **94 (8)**, 495–507, doi:10.1175/1520-0493(1966)094⟨0495:MSOALE⟩2.3.CO;2.

Rasmussen, R., and Coauthors, 2012: How well are we measuring snow: The noaa/faa/ncar winter precipitation test bed. *Bulletin of the American Meteorological Society*, **93 (6)**, 811–829, doi:10.1175/BAMS-D-11-00052.1.

Reeves, H. D., and D. T. Dawson, 2013: The dependence of qpf on the choice of microphysical parameterization for lake-effect snowstorms. *Journal of Applied Meteorology and Climatology*, **52 (2)**, 363–377, doi:10.1175/JAMC-D-12-019.1.

Reinking, R. F., and Coauthors, 1993: The lake ontario winter storms (lows) project. *Bulletin of the American Meteorological Society*, **74 (10)**, 1828–1850, doi:10.1175/1520-0477-74-10-1828.

Rodi, A., 2011: King of the air: The evolution and capabilities of wyoming's observation aircraft. *Meteorological Technology International*, Surrey, United Kingdom, UKIP Media and Events, 44–47, available online at http://viewer.zmags.com/publication/852ec8f8#/852ec8f8/46.

Ryzhkov, A. V., T. J. Schuur, D. W. Burgess, P. L. Heinselman, S. E. Giangrande, and D. S. Zrnic, 2005: The joint polarization experiment: Polarimetric rainfall measurements and hydrometeor classification. *Bulletin of the American Meteorological Society*, **86 (6)**, 809–824, doi:10.1175/BAMS-86-6-809.

Saslo, S., and S. J. Greybush, 2017: Prediction of lake-effect snow using convection-allowing ensemble forecasts and regional data assimilation. *Weather and Forecasting*, **32 (5)**, 1727–1744, doi:10.1175/WAF-D-16-0206.1.

Schmidlin, T. W., 1993: Impacts of severe winter weather during December 1989 in the Lake Erie Snowbelt. *Journal of Climate*, **6 (4)**, 759–767, doi:10.1175/1520-0442(1993)006⟨0759:IOSWWD⟩2.0.CO;2.

Skamarock, W. C., 2004: Evaluating mesoscale nwp models using kinetic energy spectra. *Monthly Weather Review*, **132 (12)**, 3019–3032, doi:10.1175/MWR2830.1.

Steenburgh, W. J., and L. S. Campbell, 2017: The OWLeS IOP2b lake-effect snowstorm: Shoreline geometry and the mesoscale forcing of precipitation. *Monthly Weather Review*, **145 (7)**, 2421–2436, doi:10.1175/MWR-D-16-0460.1.

Steiger, S. M., and Coauthors, 2013: Circulations, bounded weak echo regions, and horizontal vortices observed within long-lake-axis-parallel–lake-effect storms by the doppler on wheels. *Monthly Weather Review*, **141 (8)**, 2821–2840, doi:10.1175/MWR-D-12-00226.1.

Vasiloff, S., 2001: Wsr-88d performance in northern utah during the winter of 1998–1999. part i: Adjustments to precipitation estimates. Tech. rep., NOAA NSSL WRH-SSD.

Veals, P. G., and W. J. Steenburgh, 2015: Climatological characteristics and orographic enhancement of lake-effect precipitation east of lake ontario and over the tug hill plateau. *Monthly Weather Review*, **143 (9)**, 3591–3609, doi:10.1175/MWR-D-15-0009.1.

Wang, Z., and Coauthors, 2012: Single aircraft integration of remote sensing and in situ sampling for the study of cloud microphysics and dynamics. *Bulletin of the American Meteorological Society*, **93**, 653–668, doi:10.1175/BAMS-D-11-00044.1.

Welsh, D., B. Geerts, X. Jing, P. T. Bergmaier, J. R. Minder, W. J. Steenburgh, and L. S. Campbell, 2016: Understanding heavy lake-effect snowfall: The vertical structure of radar reflectivity in a deep snowband over and downwind of lake ontario. *Monthly Weather Review*, **144 (11)**, 4221–4244, doi:10.1175/MWR-D-16-0057.1.

Wright, D. M., D. J. Posselt, and A. L. Steiner, 2013: Sensitivity of lake-effect snowfall to lake ice cover and temperature in the great lakes region. *Monthly Weather Review*, **141 (2)**, 670–689, doi:10.1175/MWR-D-12-00038.1.

Zhu, P., and P. Zuidema, 2009: On the use of pdf schemes to parameterize sub-grid clouds. *Geophysical Research Letters*, **36 (5)**, doi:10.1029/2008GL036817.

LIST OF TABLES

TABLE 1. Twenty-two hour liquid-equivalent precipitation (in mm) at Sandy Creek and North Redfield from d03, d04 (WRF-LES), the KTYX Level II radar reflectivity, 6-h surface observations disaggregated with KTYX Level II radar reflectivity (see Campbell et al. 2016, their Fig. 4) and the KTYX Level III One-Hour Precipitation (DAA/170).

	Sandy Creek	North Redfield
d03	24	57
d04	27	54
KTYX Level II	32	48
Disaggregated observations	32	58
KTYX Level III (DAA)	45	77

TABLE 2. Ice mass (q_{IX}) and number (n_{IX}) concentrations for all three ice species ($X = 1,2$ or 3) averaged from 1600-2000 UTC from 0-3 km AGL along leg 3 where the Doppler hydrometeor vertical velocity is greater than 1 m s^{-1} and along leg 3 and leg 5 (for all hydrometeor vertical velocities). Values are for the WRF-LES domain and are in parentheses for d03.

	Leg 3		Leg5
	w>1 m s^{-1}	all	all
q_{I1} (g m^{-3})	0.20 (0.22)	0.17 (0.14)	0.25 (0.21)
n_{I1} (L^{-1})	25.6 (18.1)	19.6 (9.8)	20.7 (12.4)
q_{I2} (g m^{-3})	0.02 (0.01)	0.02 (0.01)	0.01 (0.01)
n_{I2} (L^{-1})	3.2 (1.7)	1.8 (1.0)	1.3 (0.9)
q_{I3} (g m^{-3})	0.34 (0.52)	0.19 (0.23)	0.25 (0.32)
n_{I3} (L^{-1})	1.6 (1.4)	1.5 (1.0)	1.6 (1.4)

TABLE 3. Percentage of each ice species at the lowest model level at Sandy Creek for d03 and the WRF-LES domain, conditionally sampled for total ice of at least 0.1 g kg^{-1}, percentage of ice-one with aspect ratios greater than 0.1, 0.25 and 0.5 for d03 and the WRF-LES domain at Sandy Creek, conditionally sampled for total ice of at least 0.1 g kg^{-1} and the percentage of 1-km AGL updrafts greater than 3 and 4 m s^{-1} at Sandy Creek.

	d03	d04
q_{I1}	26.8%	45.2%
q_{I2}	1.2%	2.8%
q_{I3}	72.0%	52.0%
ϕ_{I1}>0.1	6.3%	28.7%
ϕ_{I1}>0.25	0.0%	7.0%
ϕ_{I1}>0.5	0.0%	1.0%
w_{air}>3	5.6%	6.9%
w_{air}>4	0.0%	2.8%

LIST OF FIGURES

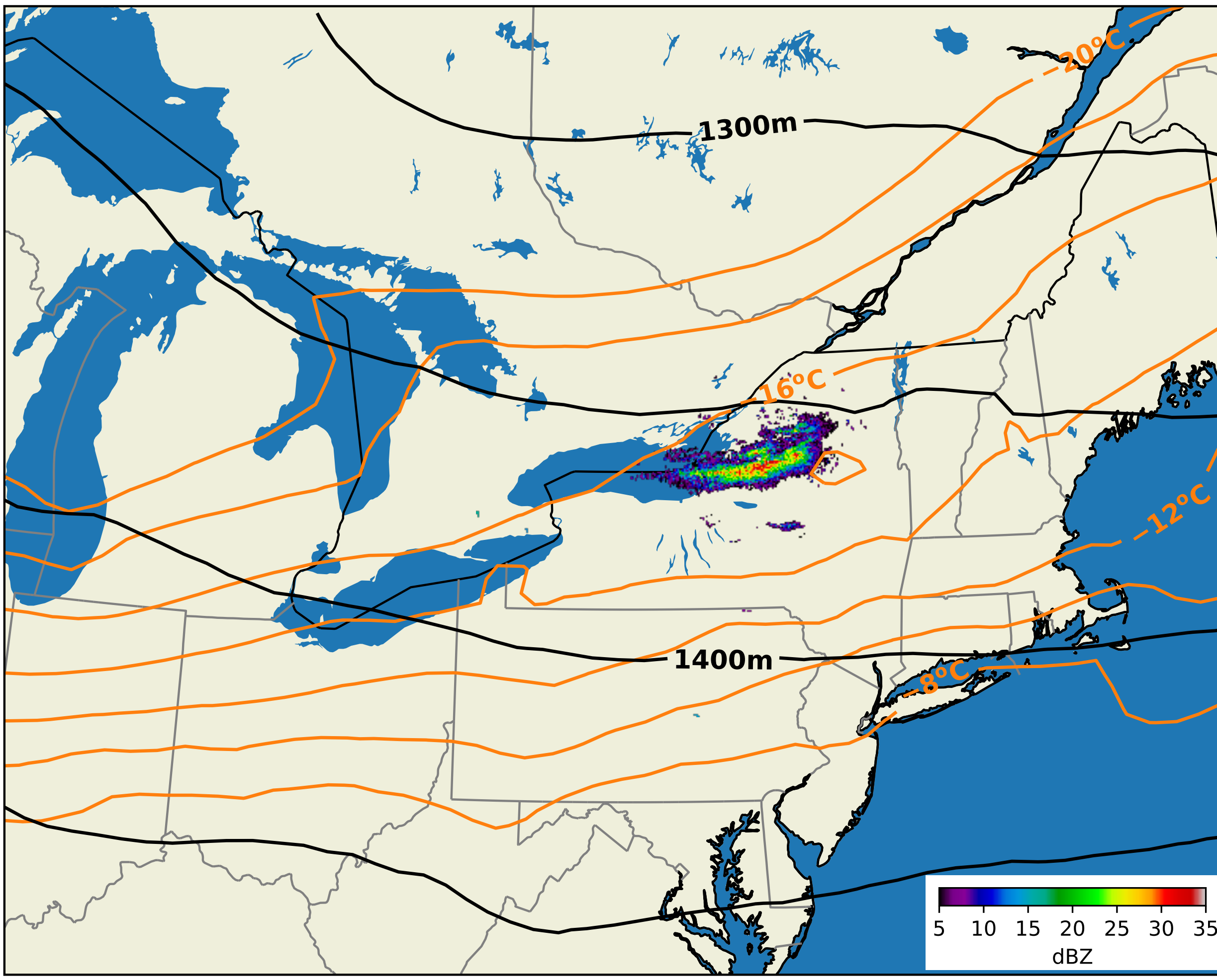

FIG. 1. KTYX radar reflectivity field at 1805 UTC 11 Dec 2013. Orange contours are 850-mb air temperatures (2 °C intervals) and black contours are 850-mb geopotential heights (50 m intervals) from the NARR.

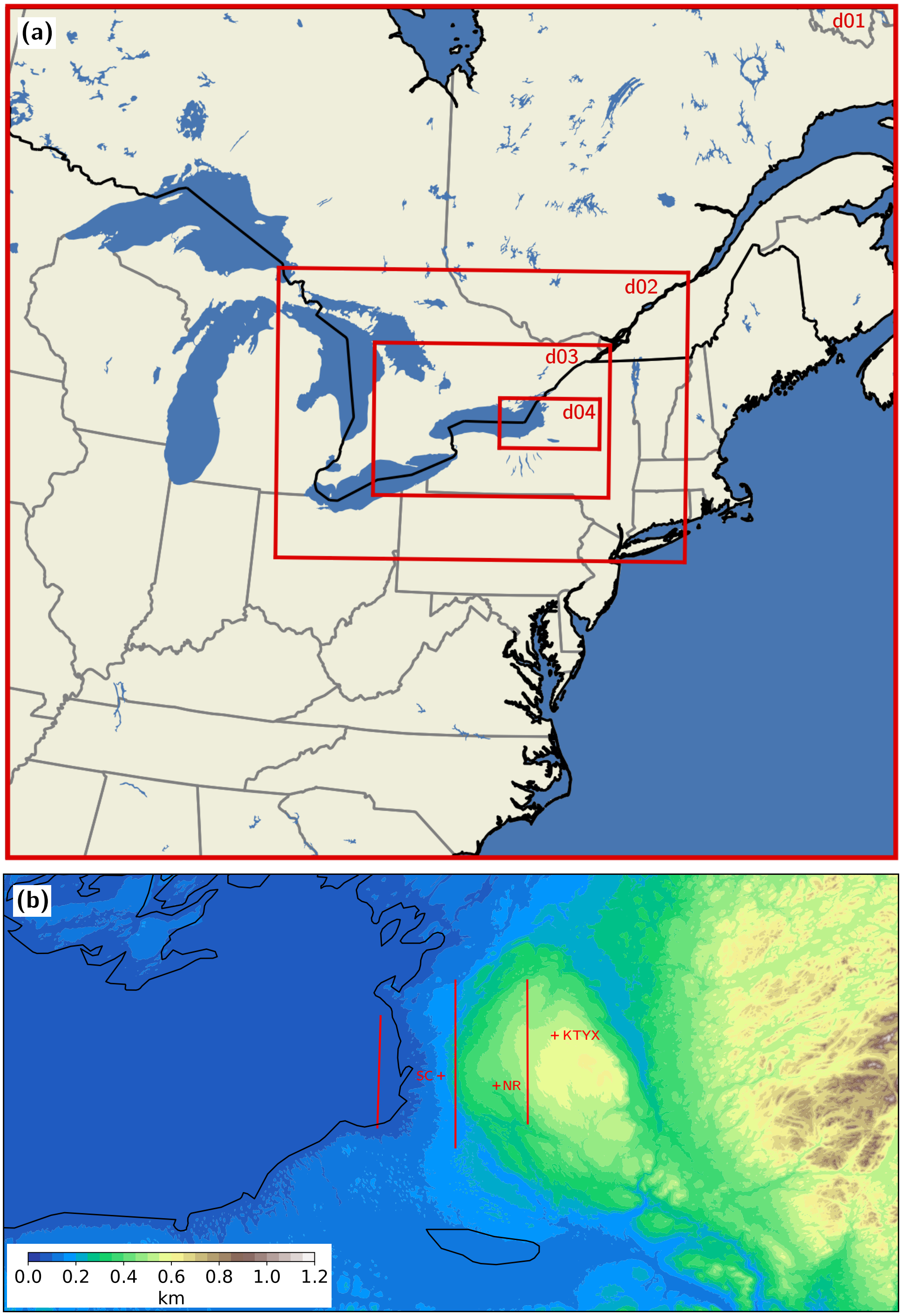

FIG. 2. The simulation domain and high-resolution terrain. (a) The all-encompassing parent domain (d01) and the 3 nests. (b) The WRF-LES domain (d04) terrain. The red lines are the flight legs 3, 4 and 5, from west to east. The red pluses show the locations of the KTYX radar, North Redfield (NR) and Sandy Creek (SC). The black contour is the outline of Lake Ontario, and Lake Oneida, south of flight legs 4 and 5, is also contoured.

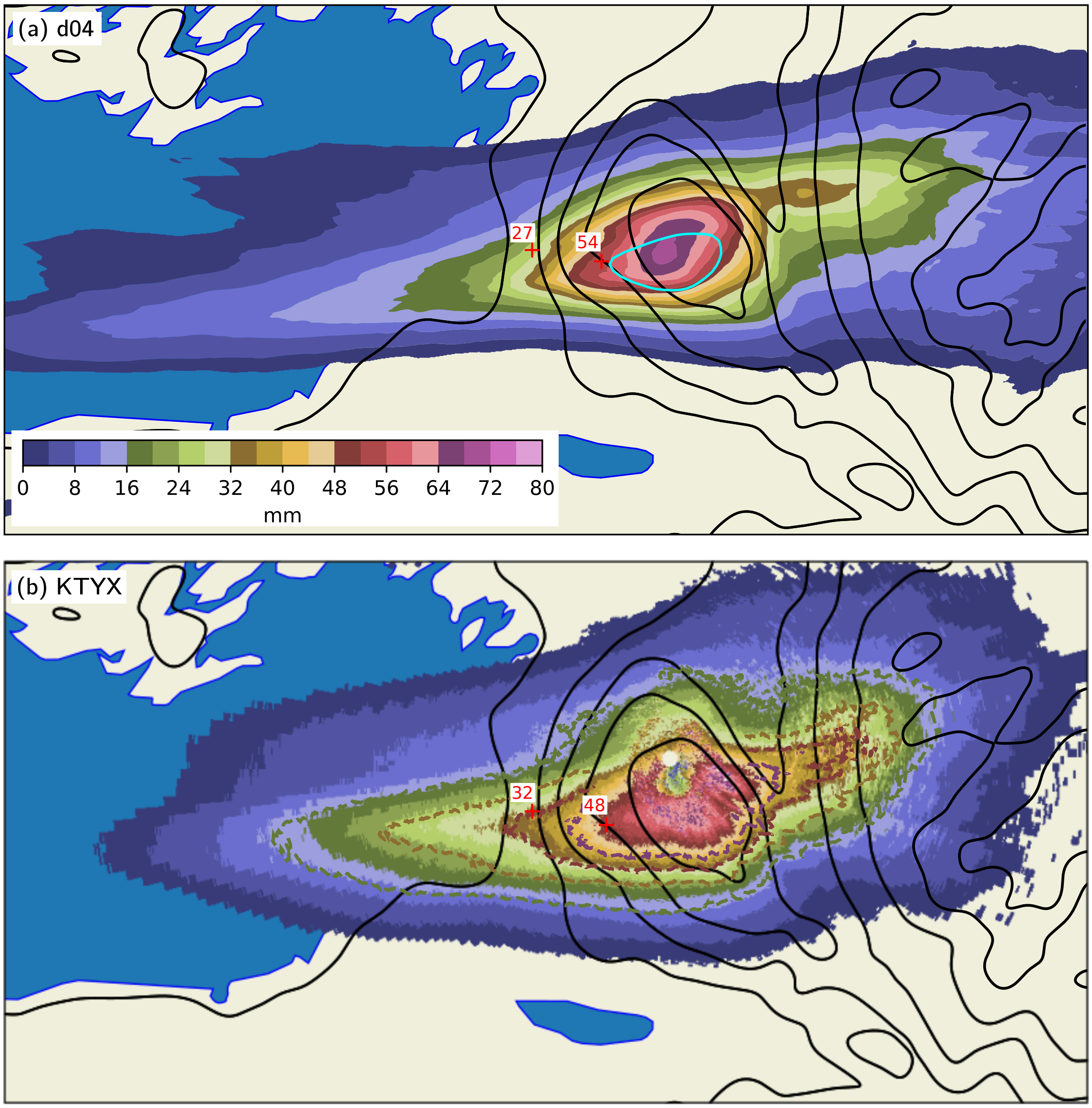

FIG. 3. 22-h (0000-2200 UTC 11 Dec 2013) liquid-equivalent accumulated precipitation (a) from the WRF-LES domain and (b) derived from the KTYX radar. The black contours are smoothed terrain heights from the WRF-LES domain (0.1 km intervals from 0.1-0.7 km). The cyan contour in (a) is the 60-mm contour from d03 (1.33-km domain). The dashed contours in (b) are the 22-h accumulated precipitation from the Level III (DAA/170) product (contours shown are 16, 32, 48 and 64 mm). The pluses show the locations of Sandy Creek and North Redfield, and their 22-h accumulations from level II KTYX data are shown.

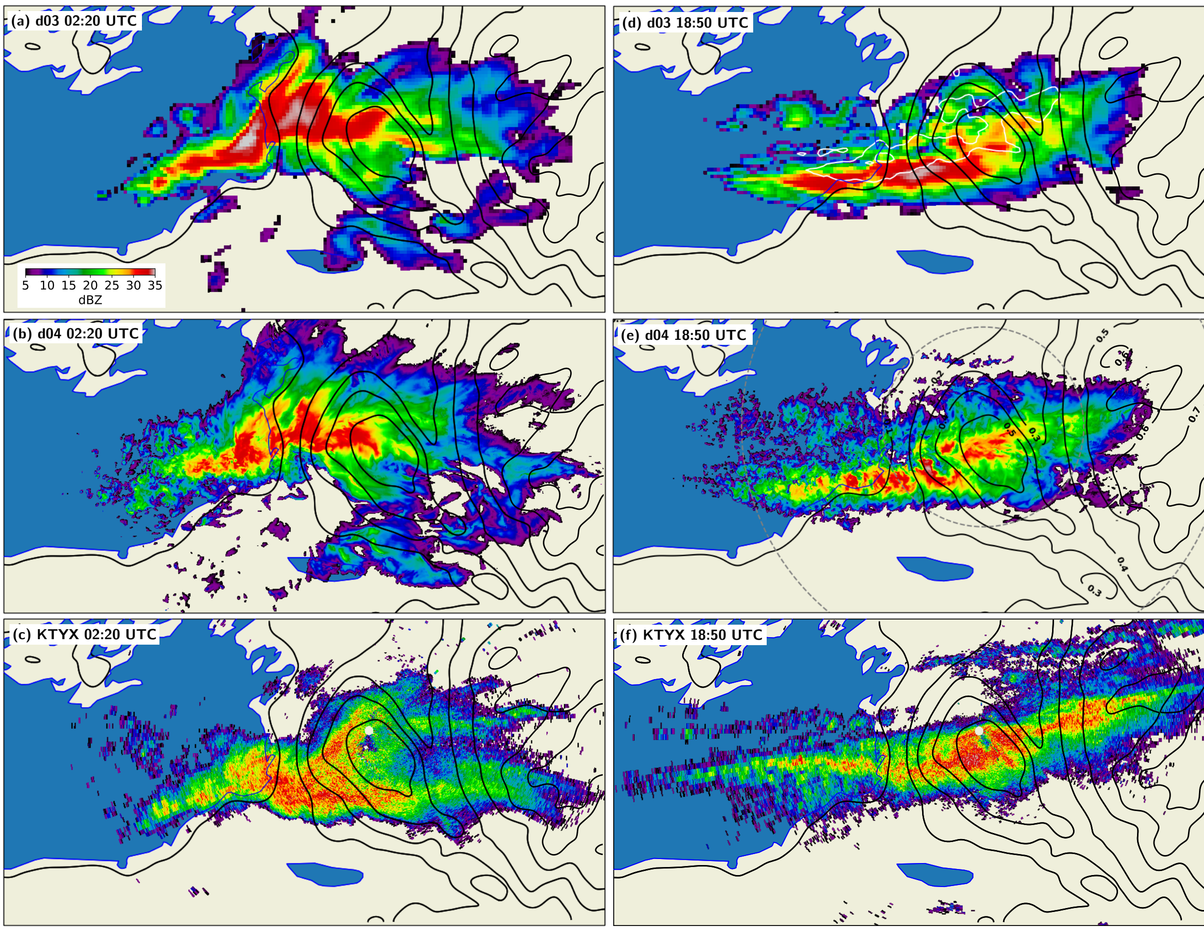

FIG. 4. Reflectivity field at 0220 UTC 11 Dec 2013 from (a) d03, (b) the WRF-LES domain, and (c) the KTYX radar. (d), (e) and (f) are the same as (a), (b) and (c) but at 1850 UTC 11 Dec 2013. The white contour in (d) is the d03 25-dBZ contour at 1600 UTC (2h 50 min earlier). The black contours, labeled in (e), in all panels are smoothed terrain heights from the WRF-LES domain. The gray, dashed circles in (e) are the 1-km and 2-km above-radar height ranges.

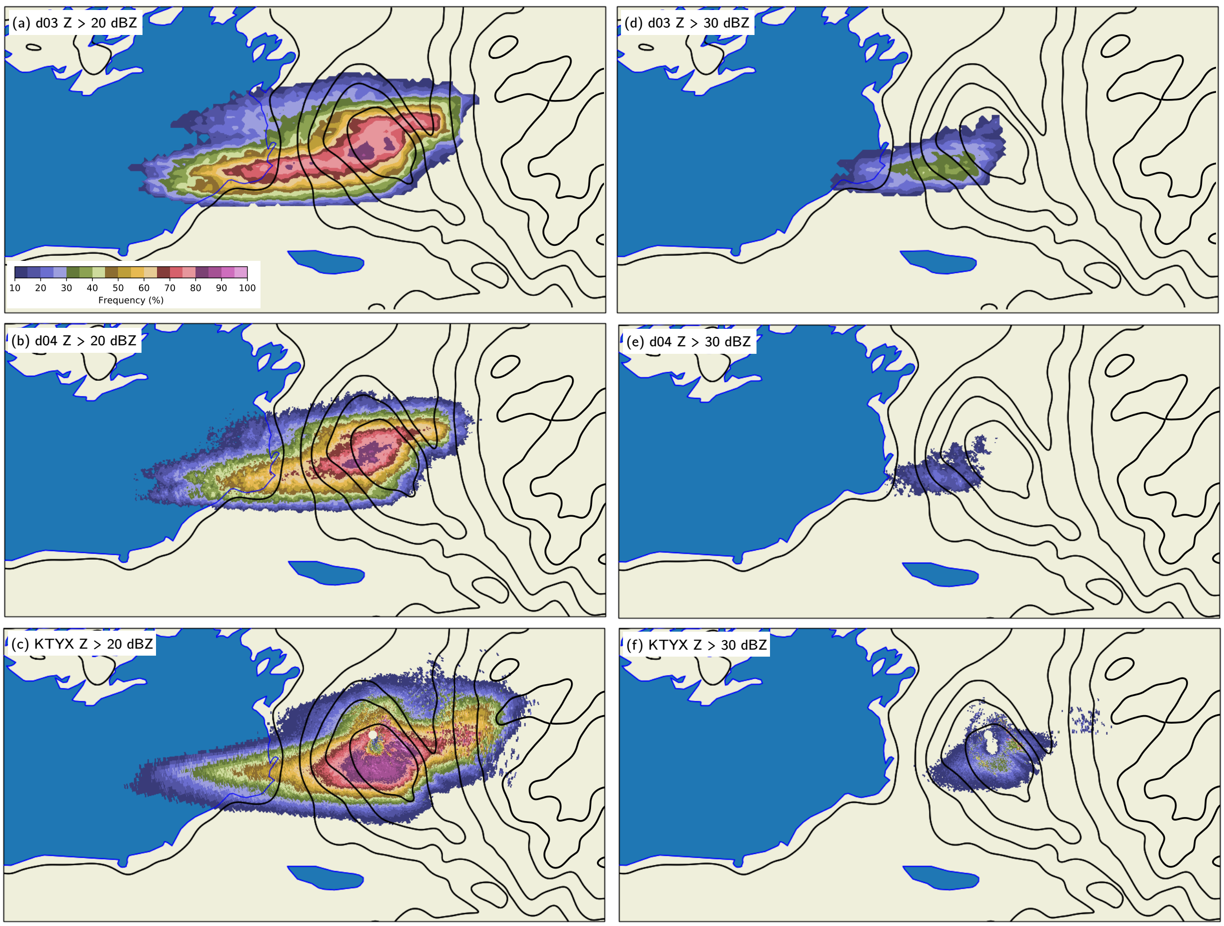

FIG. 5. 22-h (0000-2200 UTC 11 Dec 2013) frequency plot of reflectivity values greater than 20 dBZ from (a) d03, (b) the WRF-LES domain and (c) the KTYX radar. The black contours are smoothed terrain heights from the WRF-LES domain. (d), (e) and (f) are the same as (a), (b) and (c) but for reflectivity values greater than 30 dBZ.

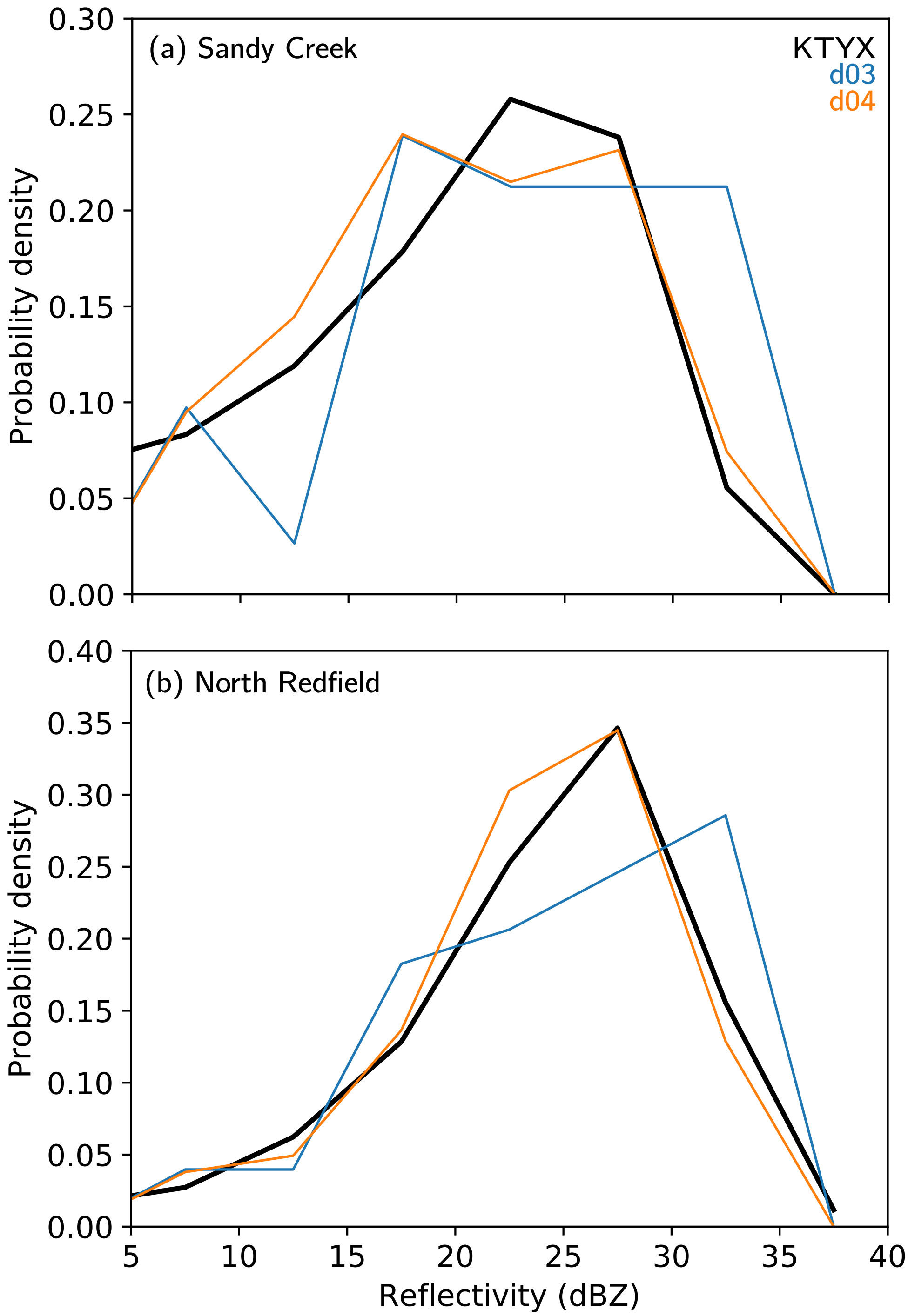

917 FIG. 6. Probability density of reflectivity values (every 5 dBZ) at (a) Sandy Creek and (b) North Redfield for
918 22 h from the KTYX radar (black), d03 (blue) and the WRF-LES domain (orange).

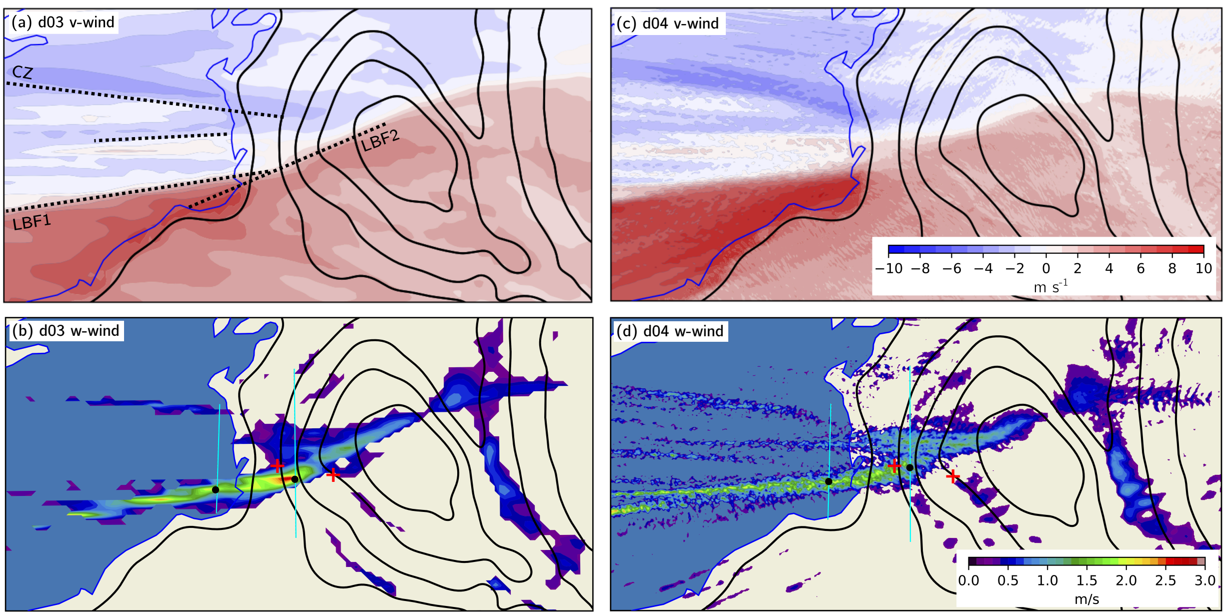

FIG. 7. Lowest model-level, grid-relative *v*-wind component averaged from 1600-1800 UTC for (a) d03 and (c) the WRF-LES domain. The dashed black lines show the land-breeze front locations (LBF1, LBF2), the northern-shore convergence zone (CZ) and the mid-lake convergence zone (unlabeled). Vertical air motion at 1 km AGL averaged from 1600-1800 UTC for (b) d03 and (d) the WRF-LES domain. Values greater than 0.25 m s^{-1} are shown. The cyan lines are legs 3 and 4, the red pluses are the locations of Sandy Creek and North Redfield and the black circles correspond to locations in Fig. 8. The black contours are smoothed terrain heights from the WRF-LES domain.

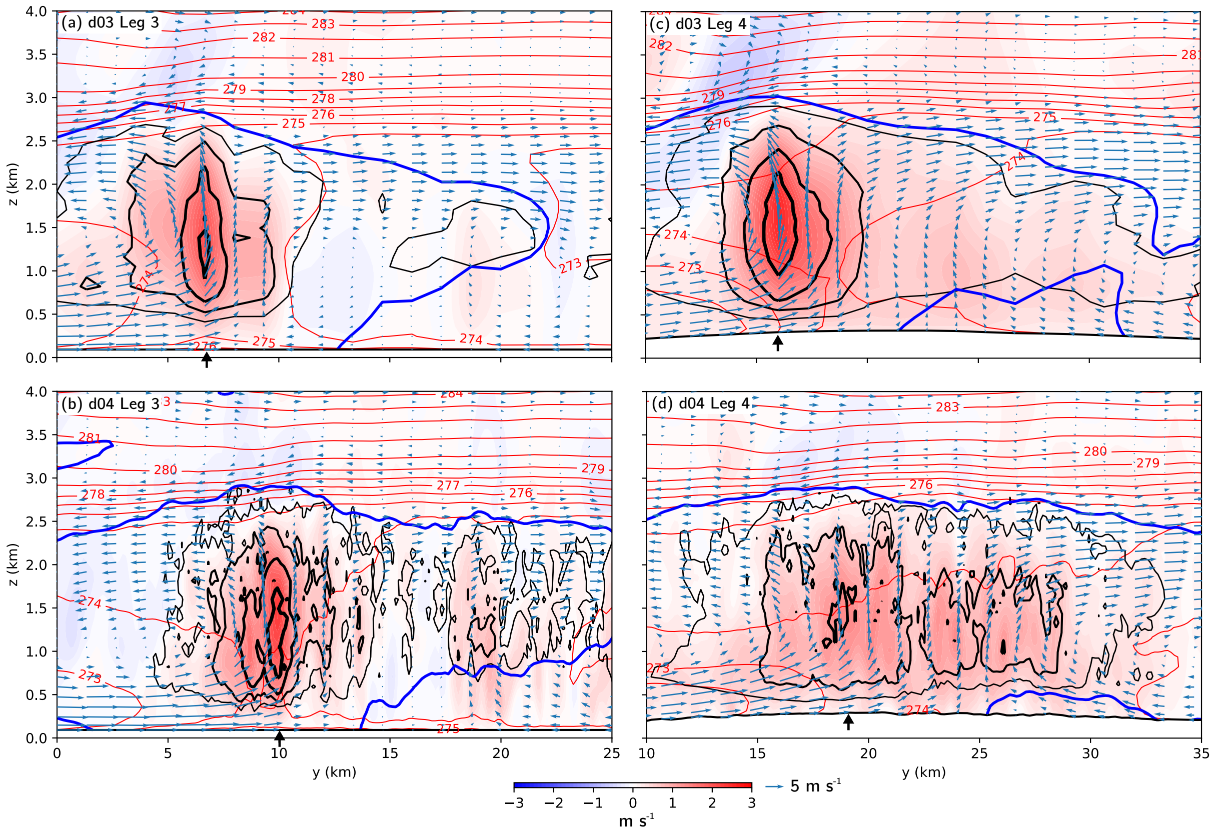

FIG. 8. Average vertical air motion from 1600-1800 UTC along leg 3 (see Fig. 2b) for (a) d03 and (b) the WRF-LES domain. The red contours are θ_e values, the blue contours are total ice mass mixing ratios of 0.1 g kg^{-1}, the wind vectors are the v and w_{air} (air motion only) component (w_{air} values are threefold for aesthetics) and the black contours are heating rates of 1, 5, 10 and 15 K h^{-1} (increasing from thin to thick). (c) and (d) and the same as (a) and (b) but along leg 4. The black arrows point to the locations marked by black circles in Fig. 7b, d. The left side of each panel is the southern side.

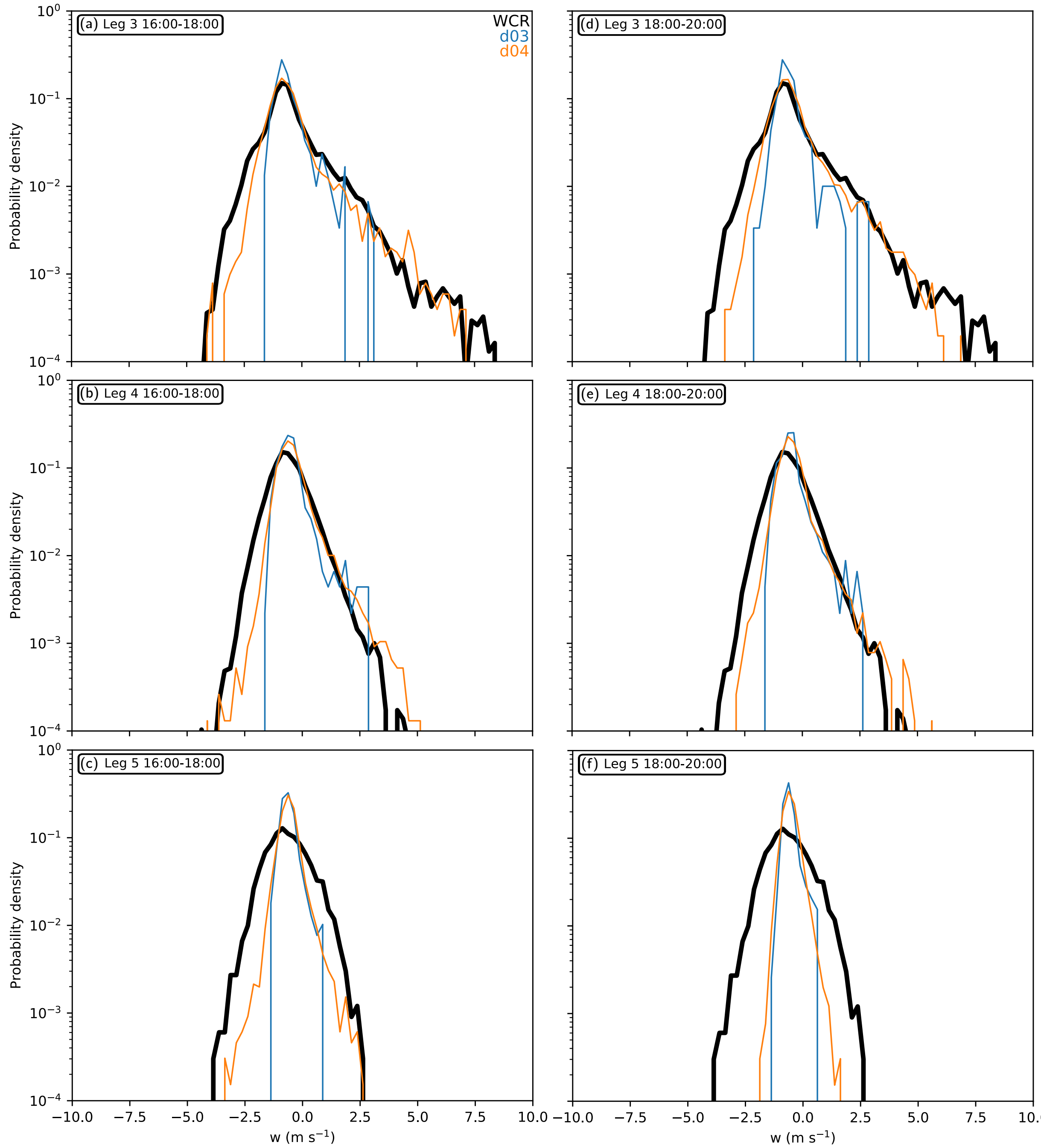

932 FIG. 9. Probability densities of Doppler hydrometeor vertical velocity at 1 km AGL from d03 (blue), the WRF-LES domain (orange), and the WCR (black) averaged from 1600-1800 UTC along (a) leg 3, (b) leg 4 and (c) leg 5. (d), (e) and (f) are the same as (a), (b) and (c) but averaged from 1800-2000 UTC.

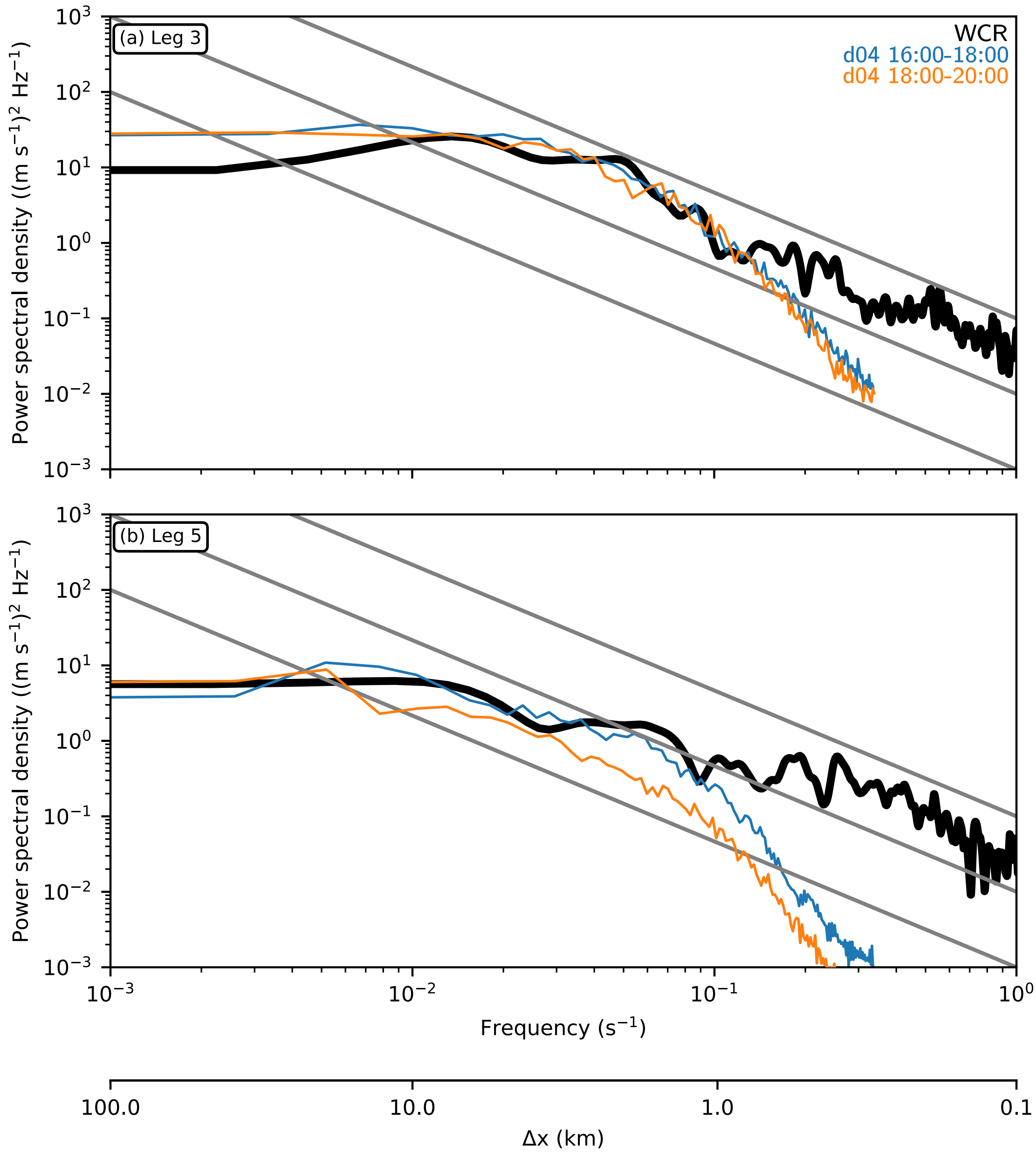

935 FIG. 10. Power spectral density of Doppler hydrometeor vertical velocity from the WCR (filtered, black), the
936 WRF-LES domain averaged from 1600-1800 UTC (blue) and averaged from 1800- 2000 UTC (orange) along
937 leg 3 at 1 km AGL. (b) is the same as (a) but along leg 5. The slopes of the gray lines are $-5/3$.

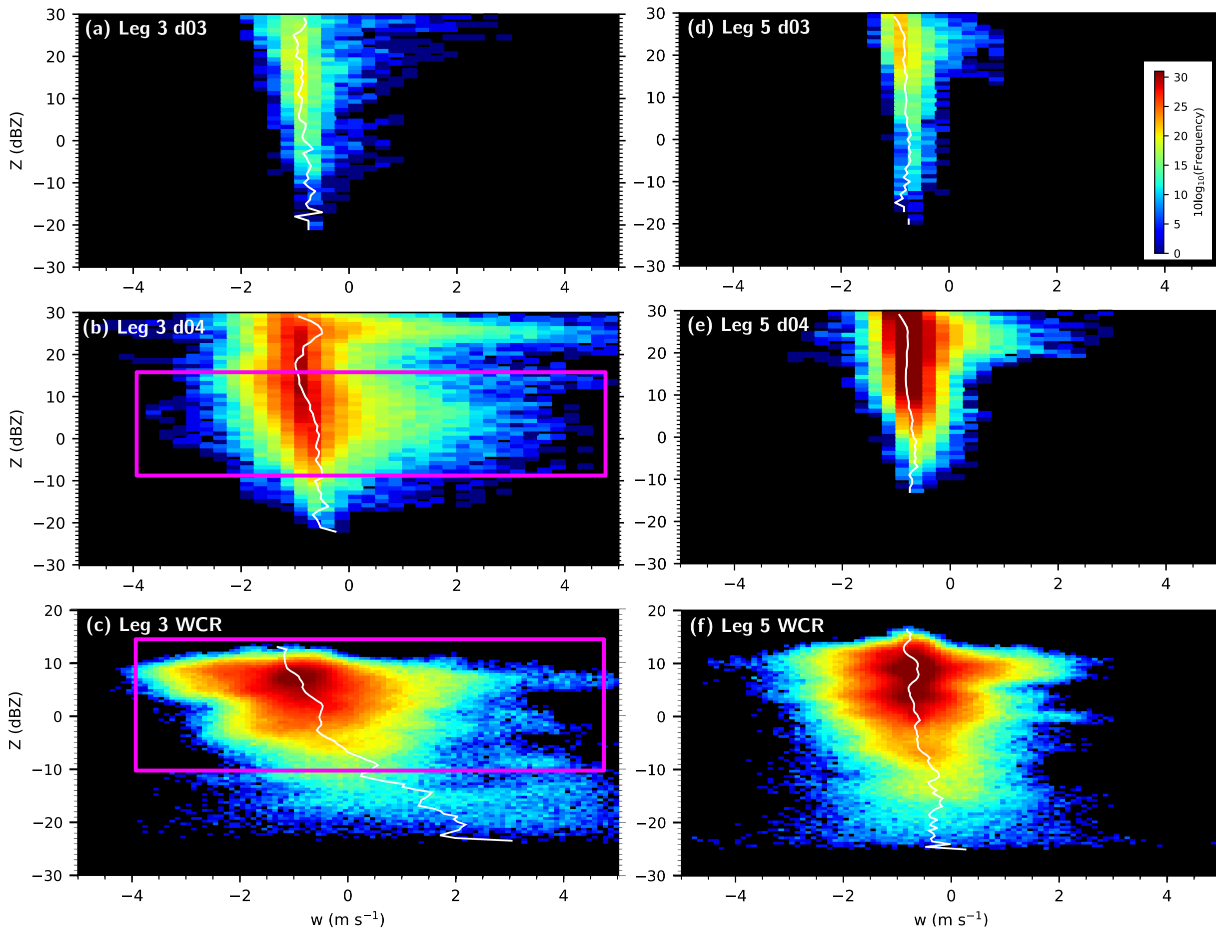

FIG. 11. Frequency plots of reflectivity versus hydrometer vertical velocity from 1600-2000 UTC and from the surface to 1 km AGL along leg 3 for (a) d03, (b), the WRF-LES domain and (c) the WCR. (d), (e) and (f) are the same as (a), (b) and (c) but along leg 5. The white lines show the averages and the magenta boxes show the same region of Z and w.

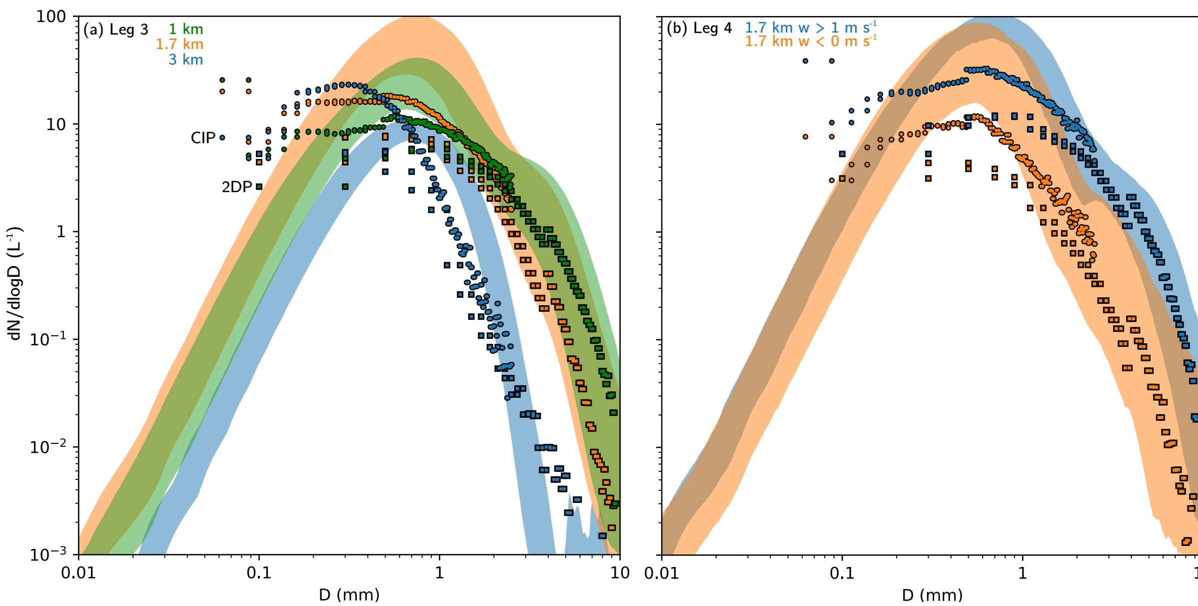

FIG. 12. Ice particle size distributions from 1600-1800 UTC along (a) leg 3 from the WRF-LES domain at 1 km MSL (green), 1.7 km MSL (orange) and 3 km MSL (blue). The shaded regions bracket the 25-75 percentile of all ice size distributions from the model along the leg during the time period. The circles are the aircraft CIP data and the squares are the 2DP data, colored by the same altitude as used for the model output. (b) is the same as (a) but along leg 4 at 1.7 km MSL and conditionally sampled for $w > 1$ m s^{-1} (blue) and $w < 0$ m s^{-1} (orange).

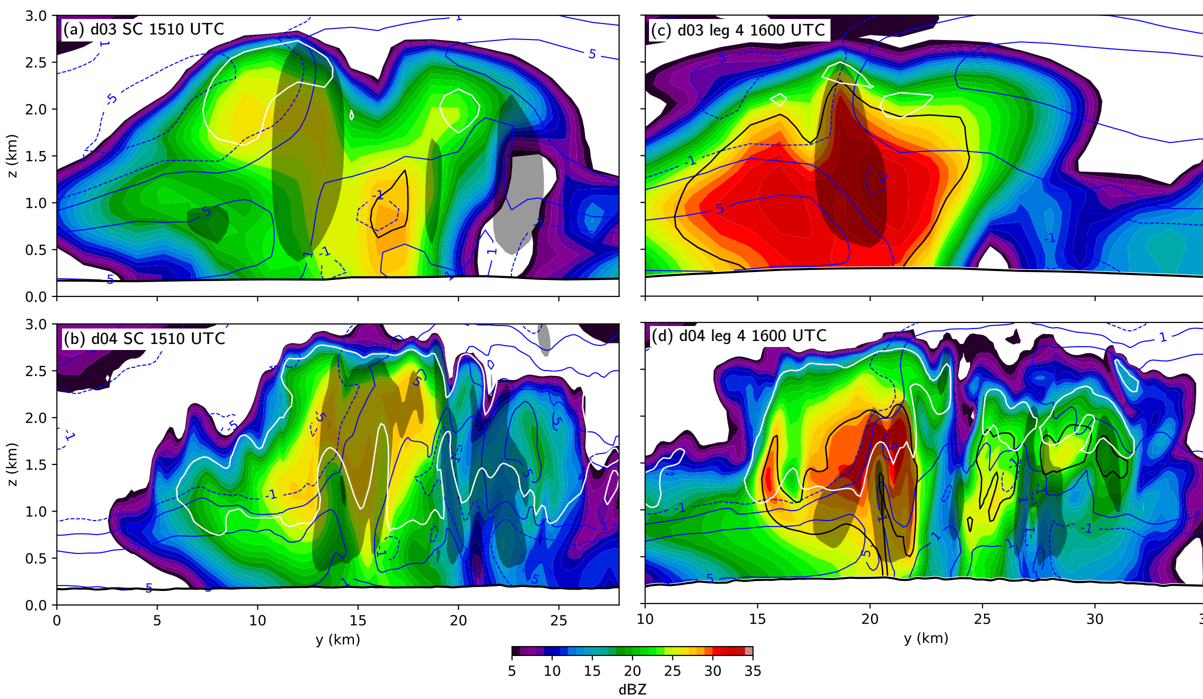

FIG. 13. Reflectivity field along a north-south cross-section through Sandy Creek at 1510 UTC for (a) d03 and (b) the WRF-LES domain. The blue contours are the v-wind component (labeled in m s^{-1}), dashed (negative) are northerly. The filled light gray contours are where $w_{air} > 1$ m s^{-1} and the filled dark gray contours are where $w_{air} > 5$ m s^{-1}. The black contours are aggregate mass concentrations of 0.5 g m^{-3} and the white contours are ice-one number concentrations of 50 L^{-1}. (c) and (d) are the same as (a) and (b) but at 1600 UTC along leg 4. The left side of each panel is the southern side.

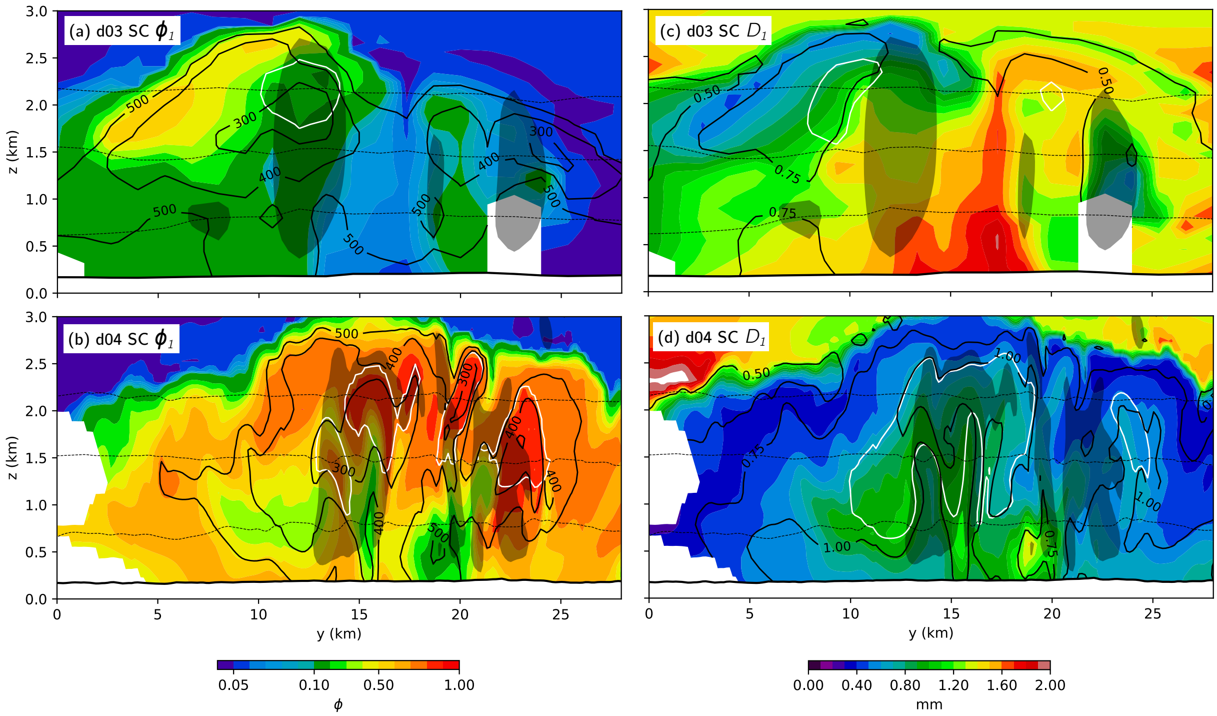

954 FIG. 14. Ice-one aspect ratios along a north-south cross-section through Sandy Creek at 1510 UTC for (a) d03 and (b) the WRF-LES domain. The white contours are riming rate of 0.0005 g m^{-3} s^{-1}, the dashed black contours are temperatures of $-10\,^{\circ}$C, $-15\,^{\circ}$C and $-20\,^{\circ}$C. The black contours are ice-one densities (labeled in kg m^{-3}). Ice-one mass-weighted maximum diameter along a north-south cross-section through Sandy Creek at 1510 UTC for (c) d03 and (d) the WRF-LES domain. The white contours are ice-one mass concentrations of 1 g m^{-3}. The dashed black contours are temperatures of $-10\,^{\circ}$C, $-15\,^{\circ}$C and $-20\,^{\circ}$C. The black contours are ice-one mass-weighted fall speeds (labeled in m s^{-1}). The left side of each panel is the southern side.

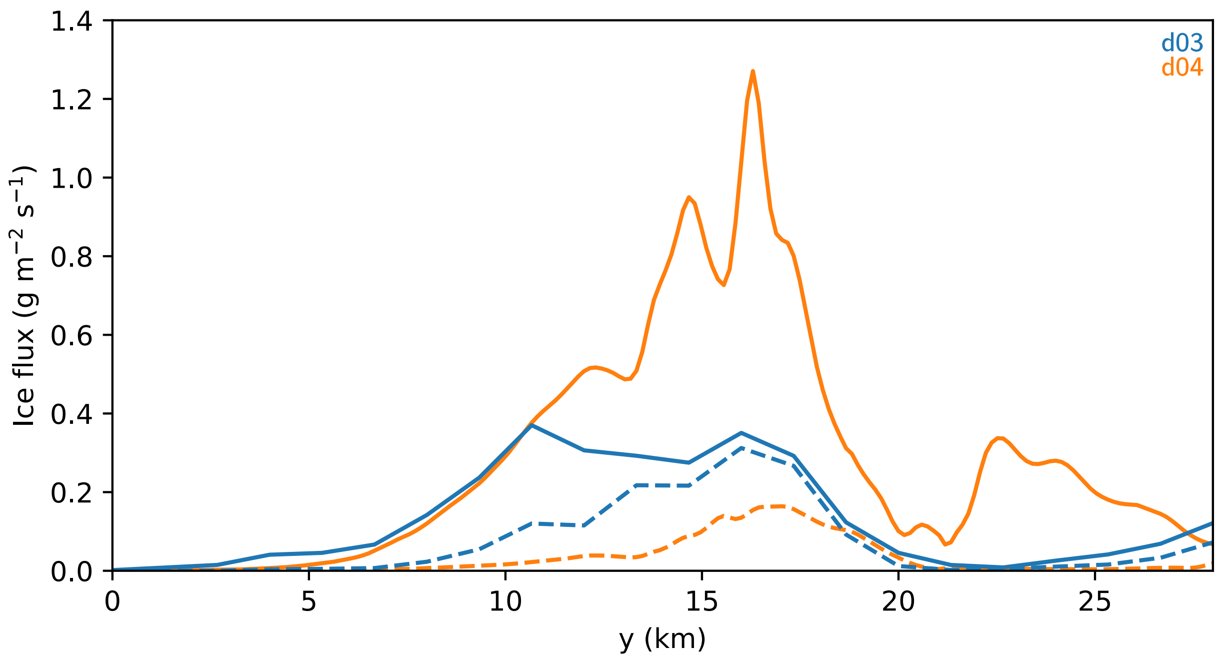

FIG. 15. Lowest model level total vertical ice mass flux along the cross-section shown in Fig. 14 from d03 (blue) and the WRF-LES domain (orange). The mass flux of aggregates is shown as the dashed lines. The left side of the figure is the southern side.

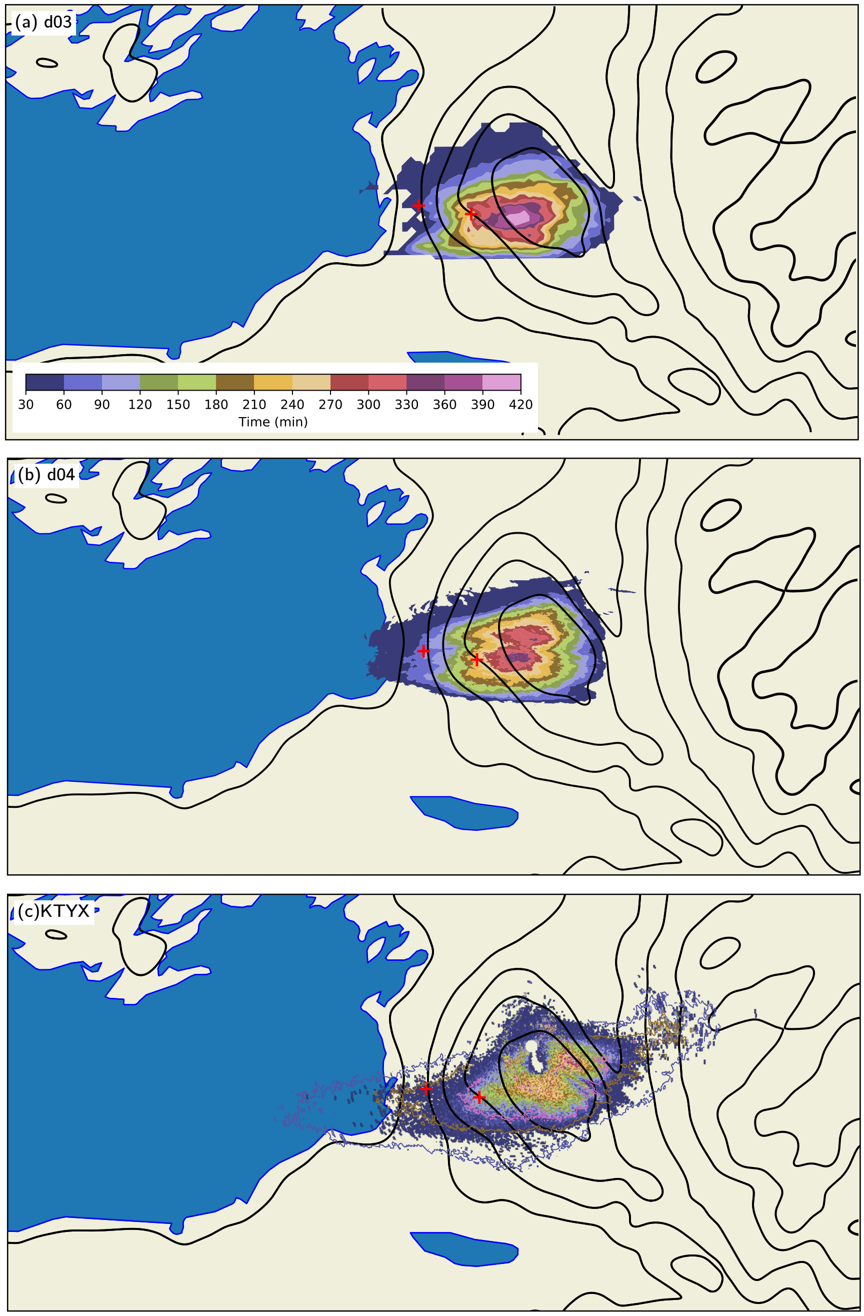

FIG. 16. Time in minutes in which liquid equivalent precipitation rates are greater than 4.23 mm h^{-1} (2 inches h^{-1} of snowfall assuming a 12-1 snow-to-liquid ratio) from (a) d03, (b) the WRF-LES domain and (c) the KTYX radar. Only values greater than 30 min are shown. The contour lines in (c) are calculated from the Level III (DPR/176) product (contours shown are 60, 180 and 360 minutes). The black contours are smoothed terrain heights from the WRF-LES domain. The locations of Sandy Creek and North Redfield are shown as red pluses.